

Synthesis and properties of $\text{YBa}_2\text{Cu}_3\text{O}_{7-x}$ thin films grown in situ by 90° off-axis single magnetron sputtering

C.B. Eom^{a,b,c}, J.Z. Sun^a, B.M. Lairson^b, S.K. Streiffer^b, A.F. Marshall^c, K. Yamamoto^c, S.M. Anlage^a, J.C. Bravman^b and T.H. Geballe^a

^a Department of Applied Physics

^b Department of Materials Science and Engineering

^c Center for Materials Research, Stanford University, Stanford, CA 94305, USA

S.S. Laderman, R.C. Taber and R.D. Jacowitz

Hewlett-Packard Co., Palo Alto, CA 94304, USA

Received 29 June 1990

Revised manuscript received 16 August 1990

High quality superconducting films of $\text{YBa}_2\text{Cu}_3\text{O}_{7-x}$ were deposited in situ using single target 90° off-axis sputtering. We have investigated their superconducting DC and RF properties, their normal state properties, and their microstructures. These films are distinctly different from bulk crystals and post-deposition annealed films. Sharp superconducting transition temperatures can be reproducibly obtained by control of deposition parameters. The T_c can be varied from 75 to 89 K. The optimization of properties other than T_c and the control of film texture occur under conditions different from those for which the highest T_c is obtained. Normal state conductivities are as high as or higher than those of single crystals. Critical current densities reach 6×10^7 A/cm² at 4.2 K. All the above properties are relatively insensitive to compositional variations. The T_c 's have a much weaker dependence on the *c*-axis lattice parameters than do those of bulk samples. The measured low-temperature penetration depth is 1400 Å and surface resistance at 4.2 K and 10 GHz is as low as 16 μΩ. Microstructural studies show sharp interfaces between films and their substrates and a variety of defect structures. Many of the properties of in situ films can be explained by clean grain boundaries and the characteristics of the surface growth occurring during in situ deposition.

1. Introduction

Among the high- T_c superconductors, $\text{YBa}_2\text{Cu}_3\text{O}_{7-x}$ is a promising material for making in situ thin films and therefore an interesting system to study. The methods which have been successfully used to make $\text{YBa}_2\text{Cu}_3\text{O}_{7-x}$ in situ films include laser ablation [1,2], evaporation [3,4], composite target sputtering [5–7] and molecular beam epitaxy [8].

Composite target sputtering can be a very reproducible and easily controllable technique. However, under standard conditions, severe backspattering of the substrate by high-energy particles (O^- , high-energy O) causes compositional changes in the film. Several groups [9,10] have used non-stoichiometric targets to compensate for the selective back sputtering effect. Alternatively, Li et al. [5] have sputtered

from a stoichiometric target at high pressure (600 mTorr) and high temperature (770–850°C). The frequent collisions at high pressure result in a reduction of the kinetic energy of the particles and consequently a reduction of back sputtering. This approach also enables the use of high oxygen pressure for in situ film growth. The uniformity of the resulting film is usually poor. However, better uniformity has recently been obtained by the same group by using a hollow cathode sputter gun [11]. Sandstrom et al. [6] have used off-axis sputtering, in which substrates are placed on the side of, and at an angle to, the sputter gun. They used low pressures (6 mTorr), a rotating substrate block to obtain uniformity, and an off-stoichiometric target adjusted to improve the film composition. Even so, the T_c 's of these in situ films were broad and had low onsets.

We have developed a high-pressure, 90° off-axis sputter technique in which almost the exact composition of the target is obtained over large areas without a need for substrate block rotation [7]. Films with reproducible and in many ways excellent superconducting properties are obtained which, as will be detailed below, have some characteristics that are distinctly different from those of bulk samples and post-annealed films [7]. By monitoring the target self-bias voltage, we have also investigated [12] the behavior of negative oxygen ions, the main species of high-energy particles produced from the sputtering target. The off-axis method employed benefits both from high pressure and off-axis geometry as we will discuss below.

The in situ process described above has been standardized at Stanford since the summer of 1988 [7]. In this paper, we make a comprehensive comparison of the structure and microstructure, the DC and RF superconducting properties, and the normal state resistance of these films, each as a function of growth parameters. Initially the films were characterized by measurements of resistance vs. temperature and the resistance-determined superconducting transition. By now there are many other properties which have been measured in both the superconducting and the normal state. It will be shown that optimization of one characteristic, for instance T_c , does not guarantee optimization with respect to others, for example surface resistance. The ability to control different characteristics is of value in producing model systems for testing theory as well as for obtaining better performance of devices. The term *in situ* means that the $\text{YBa}_2\text{Cu}_3\text{O}_{7-x}$ phase is formed during growth. The formation takes place on the surface plane of the film in the presence of an incoming flux of atoms and ions, except for the final oxygen occupancy which takes place during the cool-down. Typical rates are such that it takes several seconds to deposit a monolayer. The temperature must be high enough during that time so that the mobility of the constituents is sufficiently great to allow them to order on their respective lattice sites. If the temperature is too high there is the possibility of reaction with the substrate or re-evaporation, decomposition or even antisite disorder driven by entropy. If the temperature is too low there is not enough time for the atoms to order. It has been found for many sub-

strates that there is a range of temperatures and oxygen pressures which permit good growth. Before on-composition in situ processes were introduced the highest quality superconducting films were deposited at or near room temperature with the correct composition, but with disordered or amorphous phases. A post-deposition annealing process was required to produce the desired crystalline films. In favorable cases the latter process may occur via solid state epitaxy in which the atomic mixture is raised to high enough temperatures to cause crystallization to occur, starting at the interface with the substrate.

As a rule, thin films of high- T_c superconductors grown in situ are superior to post-annealed films in terms of epitaxy, surface smoothness, and the reduction of substrate interdiffusion. The lower growth temperature allows a wider variety of substrates to be used.

2. Synthesis

The thin films were deposited using a planar magnetron sputter gun with a reduced gap between cathode and anode, allowing it to be operated at high pressure [13]. The sputter gun was mounted in a cryopumped vacuum chamber; without bake-outs, the base pressure was 2×10^{-6} Torr. Stoichiometric 2 in. diameter targets were initially prepared from "freeze dried" powders using the method developed by Johnson et al. [14]. In the latter part of the work the targets were obtained commercially [15]. The sputtering atmosphere varied between 10–100 mTorr O_2 (or N_2O) and 40–300 mTorr Ar. An RF power of 125 W generated a cathode self-bias of -50 to -75 V and gave a deposition rate for the off-axis geometry of about 0.2–0.5 Å/s, depending on the total pressure and Ar/ O_2 ratio. The self-bias voltage is related to the oxygen partial pressure and negative ion generation [12]. For most of the depositions, a radiation heater constructed from a Haynes alloy radiation shield and a Kanthal wire heating element was used. In the latter part of the work a compact commercial heater was installed [16]. The substrate temperature during deposition was measured by a Pt/Pt–10% Rh thermocouple inserted 1.5 in. deep into the nickel substrate block. The substrates were clamped mechanically to the block during the initial

stage of this research; later they were bonded by silver paste. The block temperature was held constant between 600–700°C ($\pm 5^\circ\text{C}$) during film growth. The actual substrate surface temperature is somewhat lower than that of the measured substrate block temperature. By measuring the surface temperature of the substrates with a thermocouple, we found a 40–70°C difference at 650°C for mechanically clamped substrates. Silver paste bonding generally reduces the temperature difference to below 40°C. The film thickness was varied from 20 to 4000 Å. Substrate materials investigated include MgO (100), SrTiO₃ (100), (110) and (111), LaAlO₃ (100), yttria stabilized zirconia (100) (YSZ), and R-plane sapphire (1 $\bar{1}$ 02). Most of the systematic studies reported here have been on MgO. After deposition, the chamber was immediately vented to 600 Torr of oxygen and the substrates were allowed to cool to room temperature.

Figure 1 shows the sputtering geometry we have used and the composition profile of the films across the 1.5 in. \times 1.5 in. block, showing a comparison of off-axis (a) and on-axis (b) geometries. This figure demonstrates the compositional variation of films in various positions. The composition was analyzed with an electron microprobe; results were verified in some cases by inductively coupled plasma spectroscopy and by Rutherford backscattering spectrometry. When we placed the substrate block facing the sputter gun in the on-axis configuration, the composition of the film was poor in Ba and Cu due to differential backscatter etching by the high energy particles. Even when a total pressure of 400 mTorr was used the composition profile was still very inhomogeneous and the 1:2:3 composition was obtained only in a very small region (less than $\frac{1}{4}$ in. \times $\frac{1}{4}$ in.). However, by going to the high pressure and 90° off-axis geometry, only a small spread in composition was found over an area of 1.5 in. \times 1.5 in. from which high quality films could be repeatedly obtained. In a typical run (40 mTorr Ar/10 mTorr O₂) with a target of composition Y₁₈Ba₃₃Cu₄₉, the measured composition of the films at the extreme positions (fig. 1(a)) varied from Y₁₉Ba₃₃Cu₄₈ (B1) to Y₁₇Ba₃₃Cu₅₀ (B6), illustrating the almost 1:1 correspondence between target and film composition. The slight variation in the composition profile is due to a combination of residual high-energy particle

bombardment and the difference in angular distribution of the different atomic species. At position B1, 1.5 in. away from the sputter gun, the high-energy beam can still be somewhat effective in the preferential sputtering of Ba and Cu from the film. By increasing the total pressure from 50 mTorr to 200 mTorr, increasing the Ar/O₂ ratio from 80% to 95%, and reducing the RF power from 125 W to 60 W, no compositional variation was detected. The slight enrichment of Ba concentration near the sputter gun at 50 mTorr and 125 W is due to the mass dependence of the angular distributions of the different species as reported by Wehner et al. [17]. The sputter profile of the heavy mass Ba is less directional than that of Y and Cu. We have found that the small and reproducible variation in concentration is useful in finding optimum growth conditions particularly for the growth of different orientations. Newman et al. [18] have shown recently, using a facility similar to that shown in fig. 1(a), that it is possible to extend the area of compositional uniformity to over 14.5 cm².

The film composition for the off-axis geometry turns out to be rather insensitive to the total pressure and the Ar/O₂ ratio. In contrast to face to face sputtering the variation in thickness (as measured by a stylus on the film edges formed by patterning) is small, typically less than 10% over the 1.5 in. \times 1.5 in. substrate block area.

Figure 2 is a phase diagram of the Y–Ba–Cu–O system based on the data summarized by Borman [19] and Hammond [20]. This diagram shows the stability of YBCO equilibrium phases with respect to the molecular oxygen partial pressure and temperature. The actual phase formation sequence during in situ growth is complicated due to the surface growth kinetics and the presence of a plasma which activates oxygen. Details of the growth process are still under investigation. It is clear, however, that the presence of the oxygen plasma enables the in situ growth to occur at lower oxygen pressures. On the other hand, the oxygenation process is affected by the growth rate which, when increased, shifts the apparent phase boundary to higher oxygen pressures.

To clarify the role of the plasma in the oxygenation process, four terminal resistivity measurements on a YBCO thin film were carried out both in molecular oxygen and in an oxygen plasma at reduced

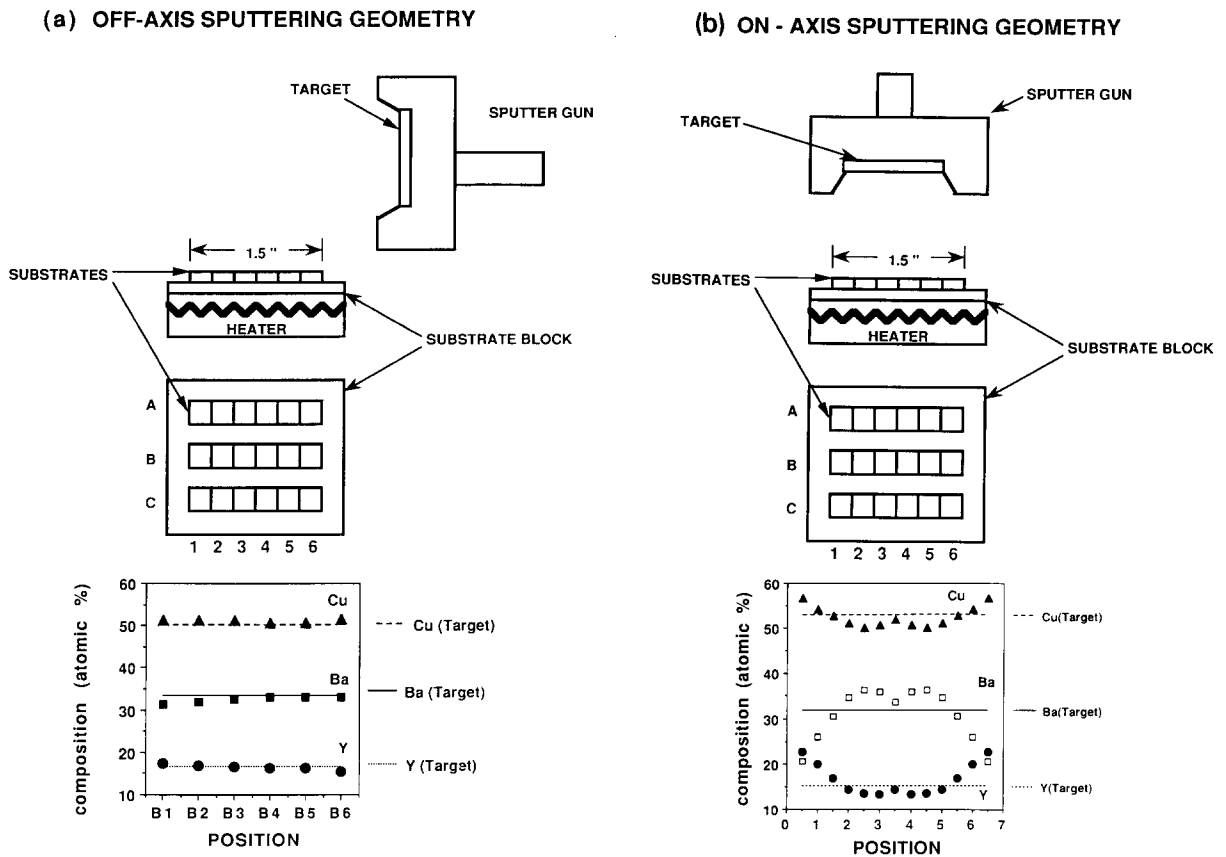


Fig. 1. Sputtering system geometry and composition profiles of the (a) off-axis and (b) on-axis geometry.

pressures. Figure 2 shows the result of such measurements. By noting the equality of the resistivities of the films at 400°C under the reactive conditions it can be seen that 10 mTorr of oxygen in the presence of a plasma is equivalent in the degree of oxidation to that of the film in 1 Torr of molecular oxygen without excitation. The plasmas can be excited either inductively or by the sputter gun itself. Thus, our operating range (P_{O_2} and temperature) is adequate for the formation of the perovskite structure. Qualitatively one would expect the presence of the excited oxygen to be effective in reducing the pressure required for perovskite formation until temperatures are reached where the dissociation of O_2 on the surface is so rapid that the species of oxygen arriving at the surface no longer matters. This occurs

for temperature above $\sim 750^\circ\text{C}$ as is shown in a detailed study of oxygen diffusion kinetics which is in progress [21].

There exists an optimum growth temperature for obtaining a given property. The optimum temperature is oxygen-partial-pressure, composition and substrate dependent. When the temperature is below a certain threshold, either unoriented or purely a -axis oriented films are formed. At somewhat higher temperatures, purely c -axis oriented films are grown. If the temperature is too high the resulting films become rich in yttrium. There also exist possible interface reactions and phase instabilities. It was found during our studies that the optimum growth temperature for both orientations (a - and c -axis) increases with increasing P_{O_2} .

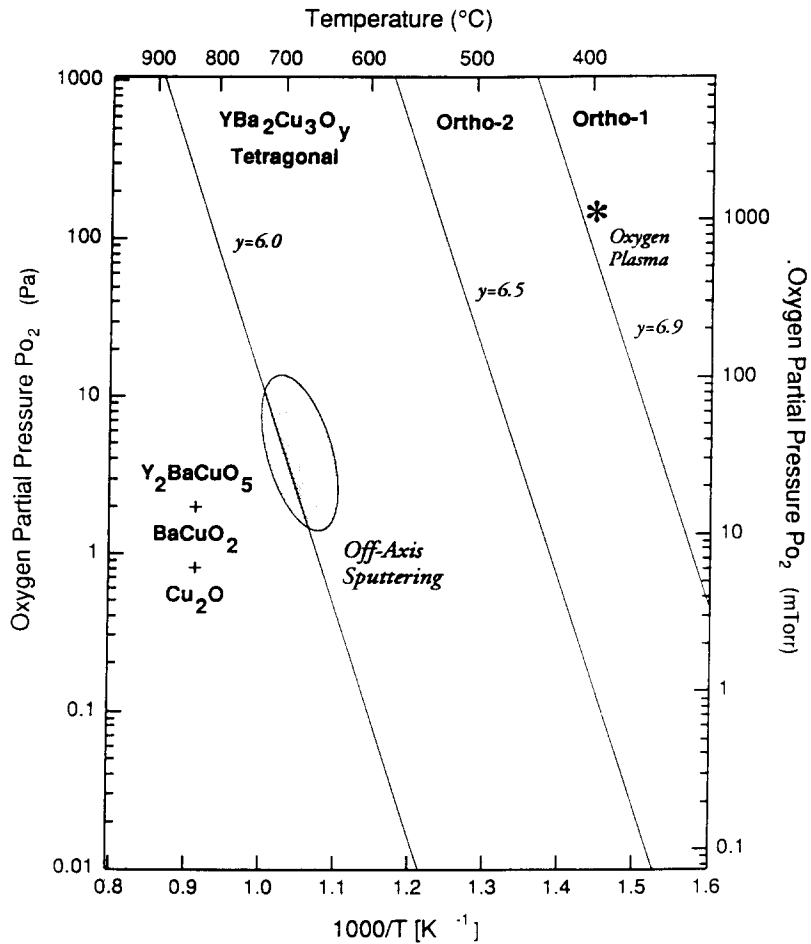


Fig. 2. Equilibrium phase diagram of the YBCO system. (R. Bormann [19] and R.H. Hammond [20]) The (*) shows that the resistivity of the YBCO thin films in 10 mTorr O_2 plasma is the same as that in 1 Torr O_2 .

3. Results and discussion

Table I lists the samples, deposition parameters and many of the properties which have been studied. Three different target composition (1:2:3, 1:2:3.5, and 1:1:2) were investigated. Many properties (resistivity, T_c , J_c , ΔT_c) are surprisingly insensitive to the overall cation compositional variations, in contrast to non-in situ grown films. While a 10% deviation from stoichiometry of post-deposition annealed films seriously degrades the critical current density and T_c [22], off-composition 1:2:3.5 and 1:1:2 films have the same T_c and only slightly degraded

critical current densities ($9 \times 10^6 \text{ A/cm}^2$, $2 \times 10^7 \text{ A/cm}^2$, respectively), at zero field and 4.2 K. The critical currents decrease only moderately with applied magnetic field. Among the substrates used in this experiment, films grown on MgO , SrTiO_3 , LaAlO_3 and YSZ all have relatively high values of T_c and J_c . Only Al_2O_3 (1 $\bar{1}$ 02) presents difficulties, due to weak epitaxy at low temperatures and interfacial reactions with YBCO at higher temperatures, resulting in a very narrow window for optimum growth. Recently, however, Char et al. [23] have shown how the use of a buffer layer deposited via laser ablation improves the quality of films grown on sapphire.

Table I
Characteristics of YBCO thin films.

Sample #	Substrate	Comp.	T_s (°C)	P_{O_2} (mTorr)	Texture	Thick (Å)	T_c (K)	ΔT_c (K)	c -axis (Å)	a -axis (Å)	$J_c(4.2\text{K})$ (A/cm ²)
<i>in situ resistivity measurement</i>											
74B5	SrTiO ₃ (100)	1:2:3.5	650	10	$c+a$	4000	86	2	11.68	3.818	
300B5	MgO(100)	1:1:2	660	10	c	4000	86	<1			2×10^7
63B5	MgO(100)	1:2:3.5	650	10	c	4000	82	1	11.74		9×10^6
<i>Textures (substrate) and SEM</i>											
27B2	SrTiO ₃ (100)	1:2:3.5	660	10	$a>c$	5000	85	3	11.72	3.82	5×10^6
152B5	SrTiO ₃ (100)	1:2:3	700	100	c	2000	86	<1	11.69	–	2×10^7
44B4	SrTiO ₃ (100)	1:2:3.5	630	10	a	3000	79	3	–	–	1×10^6
L023B4	SrTiO ₃ (110)	1:2:3	680	40	(103)	2000	86	<1	–	–	2×10^6
202B5	SrTiO ₃ (111)	1:2:3	680	40	(113)	2000	85	1	–	–	2×10^6
202B6	LaAlO ₃ (100)	1:2:3	630	10	$a(70\%)$	4000	77	3	–	–	2×10^6
L022C5	LaAlO ₃ (100)	1:2:3	700	50	c	5000	86	1	11.69	–	–
78C6	YSZ(100)	1:2:3	660	10	c	2000	84	<1	11.71	–	2×10^7
152C6	MgO(100)	1:2:3	700	100	c	2000	86	<1	11.68	–	–
152A6	Al ₂ O ₃ (1102)	1:2:3	700	100	c	2000	87	1.5	11.69	–	2×10^6
L027B5	MgO(100)	1:2:3	680	40	c	30	50	25	–	–	–
152C6	MgO(100)	1:2:3	700	100	c	1500	86	<1	11.68	–	2×10^7
86B5	MgO(100)	1:2:3	610	10	c	1500	78	2	11.79	–	2×10^7
84B5	MgO(100)	1:2:3	660	10	c	2000	84	<1	11.73	–	5×10^7
<i>TEM samples</i>											
63B5	MgO(100)	1:2:3.5	630	10	$c>a$	4000	82	1	11.75	3.82	9×10^6
123C4	MgO(100)	1:2:3	650	10	$c \gg a$	2000	82	<1	11.73	3.82	2×10^7
123B5	MgO(100)	1:2:3	650	10	$c \gg a$	2000	82	<1	–	–	2×10^7
<i>Critical current and transport measurement</i>											
182B4	MgO(100)	1:2:3	660	10	c	3000	86	<1	11.73	–	6×10^7
191A4	MgO(100)	1:2:3	660	10	c	4000	86	<1	–	–	5×10^7
191B4	MgO(100)	1:2:3	660	10	c	4000	86	<1	–	–	5×10^7
127C5	MgO(100)	1:2:3	640	10	$c \gg a$	2000	82	<1	–	–	2×10^7

3.1. Surface morphology

Surface morphology and roughness control are very important for making superconducting devices, multilayers, and ultra-thin films. Usually the morphology depends on film texture, grain size and thickness. In this work the surface morphology was investigated using scanning electron microscopy (SEM). In a few cases we were also able to obtain results from scans using an atomic force microscope (AFM) [24]. In addition, we were able to employ the AFM to observe the surface features of various substrates in order to investigate their initial condition. Sapphire and YSZ substrates, as received from the supplier and then cleaned in organic solvents, show extremely smooth surfaces having feature heights of only 1–2 Å. The surface roughness of MgO

(100) substrates depends, however, on the preparation conditions. Figure 3(a) shows the surface morphology of MgO polished at Stanford, which exhibits 3–4 Å feature heights. When MgO substrates were annealed in 1 atm O₂ at temperatures up to 1300°C the surface morphology was unchanged; however, when annealed in low O₂ pressure (~10 mTorr) at 700°C, the MgO developed a much rougher surface having 20–30 Å feature heights (fig. 3(b)).

Figure 4 shows the surface morphology of c -axis, a -axis, (103) and (113) oriented YBCO films. Films with (103) and (113) texture were grown on (110) and (113) SrTiO₃ substrates, respectively. The surfaces of c -axis oriented films are very smooth; no features could be detected within the ~200 Å resolution of the SEM. For a typical 4000 Å thick c -axis

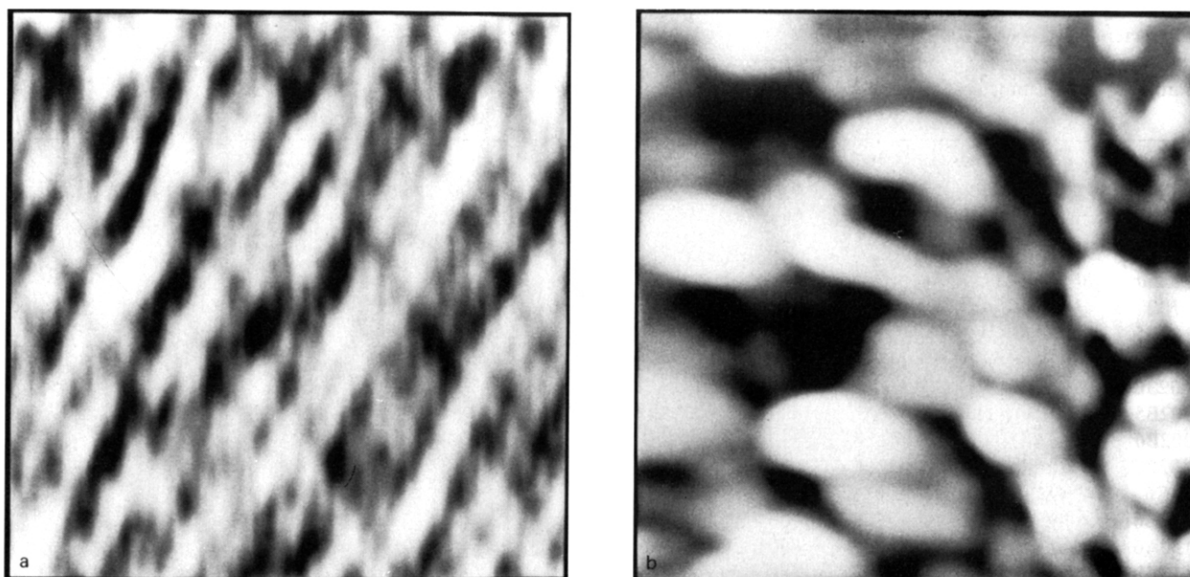


Fig. 3. Surface morphology of the MgO substrate by atomic force microscopy (AFM). (a) polished MgO (b) polished and annealed in 10 mTorr O_2 at $700^\circ C$. The contrast represents feature heights of 3–4 Å and 20–30 Å, respectively, as discussed in the text.

film on MgO, AFM images suggest a feature height of approximately 50 Å.

3.2. Transition temperature and resistivity

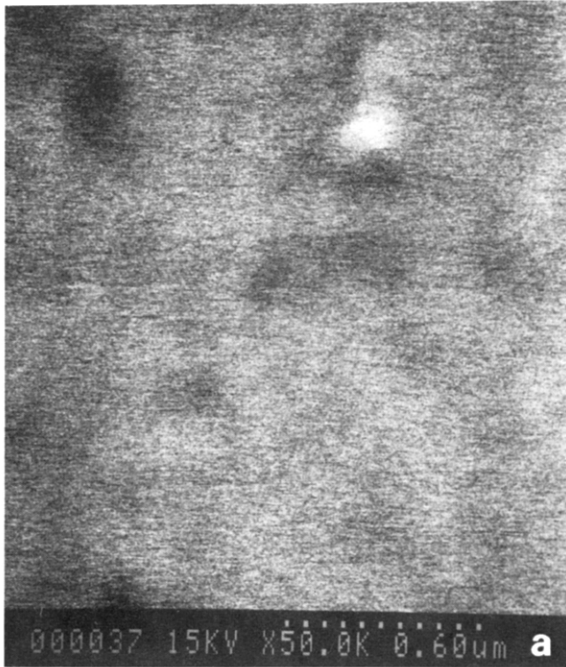
Characteristics of representative films we have studied are given in table I. Transition temperatures and normal state resistivities are measured by a four-terminal DC transport method using silver paint contacts in which the current contacts are lines and the potential leads are dots, as shown in the inset in fig. 5. Transition temperatures were verified by DC magnetic susceptibility using a SQUID magnetometer. We patterned 250 μm bridges in order to get absolute resistivities, and these resistivities were compared with results from the Van der Pauw method. The results from all measurements were found to be consistent. Thicknesses were measured by profilometry at the film edge after patterning with a 10% margin of error as discussed earlier. Although transition temperatures at zero resistivity (T_{c0}) are somewhat lower than those of bulk materials, the transition widths ΔT (defined by the temperature between the 90% value of the normal state resistivity near T_c and the temperature at zero resistivity) are

sharp; ΔT ranges from 3 K for non-optimized growth to <1 K for T_c 's varying from 75 to 89 K. Figure 5 shows representative ρ versus T transitions of films grown on MgO (100). The inset shows the narrow transition width of a high- T_c film on MgO (100). The normal state resistivity of the best films is at least as low as that of twinned single crystals [25]. From X-ray data discussed below, it is certain that this is not due to the high conductivity of the 2–4–8 phase [26]. Even for films as thin as 30 Å, the superconducting transition is still complete at 50 K, which implies a very sharp film-substrate interface with little interdiffusion. Sharp interfaces have also been seen on thicker films by cross-sectional transmission electron microscopy (TEM), as we will discuss below.

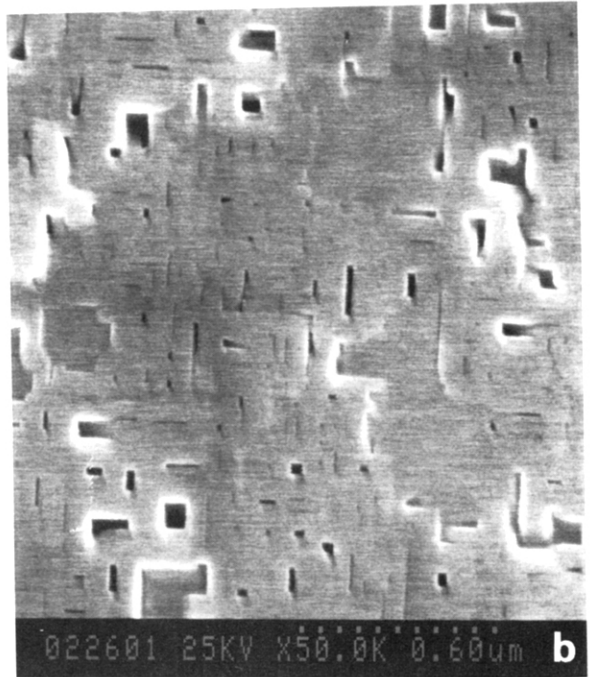
3.3. Lattice expansion and crystalline texture

The structure of the films has been studied with X-ray diffraction and transmission electron microscopy (TEM). Variations in their texture, due to different sputtering parameters and substrates, are determined with a 4-circle diffractometer with a Cu $K\alpha$ source. The results have been supplemented, when warranted, with measurements using a second four

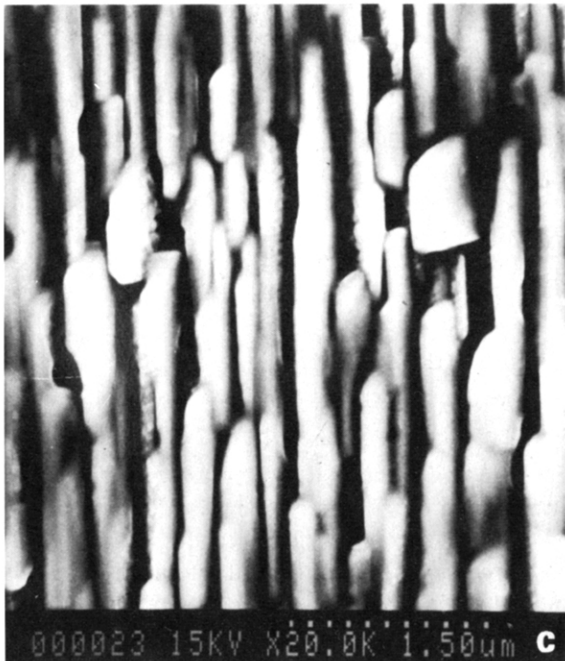
c-axis oriented film on MgO (100)



a-axis oriented film on SrTiO₃ (100)



(103) oriented film on SrTiO₃ (110)



(113) oriented film on SrTiO₃ (111)



Fig. 4. SEM micrographs of differently textured YBCO thin films on different substrates. (a) *c*-axis oriented film on MgO, (b) *a*-axis oriented films on SrTiO₃ (100), (c) (103) oriented films on SrTiO₃ (100) and (d) (113) oriented films on SrTiO₃ (111).

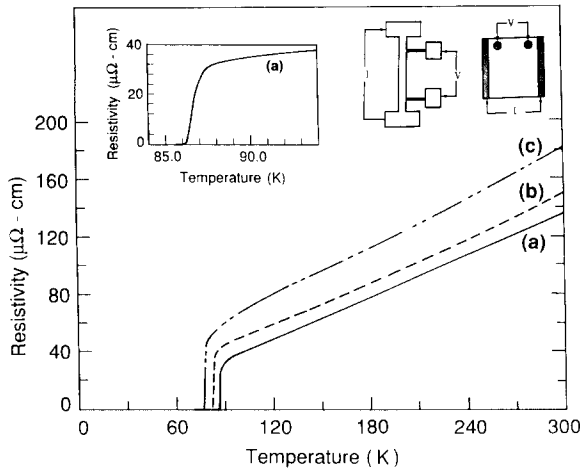


Fig. 5. Typical resistive transitions for 2000 Å thick film on MgO. (a) $T_{c0}=86.2$ K (b) $T_{c0}=82.5$ K (c) $T_{c0}=79$ K. Lower T_c films are grown at lower substrate temperatures and oxygen pressures. Insets show the geometries for the four-point resistivity measurements.

circle diffractometer, which includes incident and diffracted beam graphite monochromators and a rotating anode source operated with a copper target in a fine focused mode. In addition, we have also studied the crystalline quality of the films by measuring the rocking curve width of the (005) peak and the in-plane texture from a Φ scan of the (103) peak. The rocking curve widths were obtained using a double-crystal rocking curve apparatus (open detector) having a perfect germanium (400) first crystal. The full width at half maximum of the MgO substrates is about 0.02 deg, which is roughly an order of magnitude better than that of films deposited on them.

Purely a -axis oriented material can be obtained in slightly Cu-rich films grown at low temperature on $SrTiO_3$ (100) or $LaAlO_3$ (100) substrates. Some c -axis oriented films growth is evident on YSZ and MgO substrates under the most optimum conditions we have been able to find for a -axis growth. The textures on the (110) or (111) $SrTiO_3$ are (103) and (113), respectively. At high enough temperatures, we have grown exclusively c -axis oriented films on $SrTiO_3$ (100) and $LaAlO_3$ (100) at 1:2:3 composition. Figure 6(a,b) show the X-ray diffraction scan of c -axis and a -axis oriented films normal to the film's surface, respectively. In the earlier stage of this re-

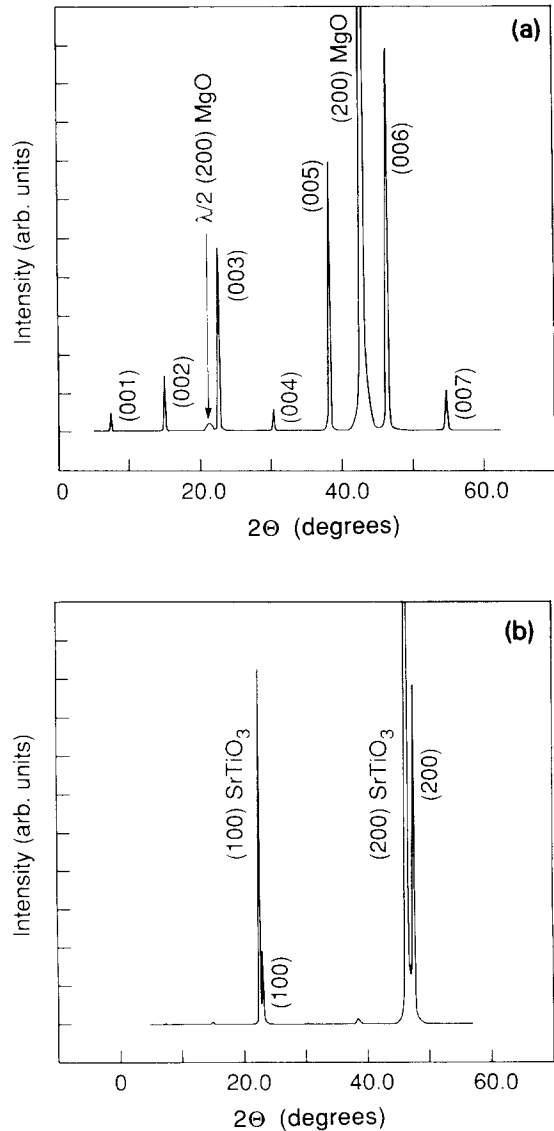


Fig. 6. X-ray diffraction pattern using Cu $K\alpha$ source showing different film textures. (a) c -axis and (b) a -axis oriented.

search it was found that some a -axis instability occurred when the film thickness was increased above 3000 Å. As the process has become optimized no evidence for any a -axis material is found even in the thickest films (>8000 Å). Impurity peaks were absent in c -axis oriented 1:2:3 samples. In many cases the high phase purity was confirmed using a slow scan and a thin film (Seeman-Bohlin geometry) diffrac-

tometer. Rocking curves (ω scan) on the YBCO (005) peak for films (152B5 and 152C6) on MgO and SrTiO_3 were both found to be 0.2° full width at half maximum (FWHM).

The X-ray data reveal an interesting relationship between the c -axis lattice parameter and the transition temperature. In fig. 7(a), the transition temperatures (T_{c0}) of films grown at various deposition temperatures and oxygen partial pressures are plotted against the c -axis lattice parameters, together with similar data obtained from studies on bulk ceramics [27,28]. This T_c versus c -axis lattice parameter ex-

pansion is also found using electron-beam evaporation as the method for in situ growth [29]. The c -axis lattice parameter increases with decreasing substrate temperature and with decreasing oxygen pressure. In our experience, the T_{c0} corresponds well with the onset of T_c measured by magnetization. Accordingly in fig. 7 we have used the published magnetic T_c onset for comparing with our resistively measured T_{c0} . It is clear from fig. 7(a) that the T_c for our in situ grown thin films has a much weaker dependence on the c -axis lattice parameters. We also measured the a -axis lattice parameters in films thicker than 2000 Å which had mixed a and c orientations. We confirmed by off-axis X-ray diffraction that the c -axis lattice parameter of a -axis grains is equal to the c -axis lattice parameter of c -axis grains on two films that contain a mixture of a and c oriented grains. This result rules out the possibility that differential thermal expansion between the film and the substrate makes a large contribution to the difference in the c -axis lattice parameters. The relation between the c -axis lattice and a -axis lattice parameters is shown in fig. 7(b). Unlike bulk superconducting ceramics where an expansion of the c -axis lattice parameter is accompanied by a similar expansion of the a -axis, our in situ films tend to have a rather constant a -axis lattice parameter even when the c -axis lattice parameter varies.

Through a series of annealing experiments (see table II), we established that the expansion of the c -axis lattice parameter was not due to oxygen deficiency in the chain site, as is the case for bulk samples. Anneals at 650°C in oxygen, for instance, caused no significant change in lattice parameters and T_c . Anneals at 850°C in oxygen, however, did increase T_{c0} to above 87 K and did shrink the c -axis lattice parameter to 11.68 Å, characteristic of bulk $\text{YBa}_2\text{Cu}_3\text{O}_7$. Such temperatures are high enough to cause recrystallization of the films [30] and thus it is not surprising that the films become more like bulk material and post-annealed films. The 400°C anneals of as-grown in situ films in 10 mTorr of oxygen show depletion of oxygen from the films; the T_c was degraded to around 30 K, and the c -axis and a -axis lattice parameters expanded significantly, closely approaching the bulk values for the same T_c (fig. 7). Subsequent 400°C anneals of the same films in 1 atm oxygen restored T_c and the c - and a -axis lattice pa-

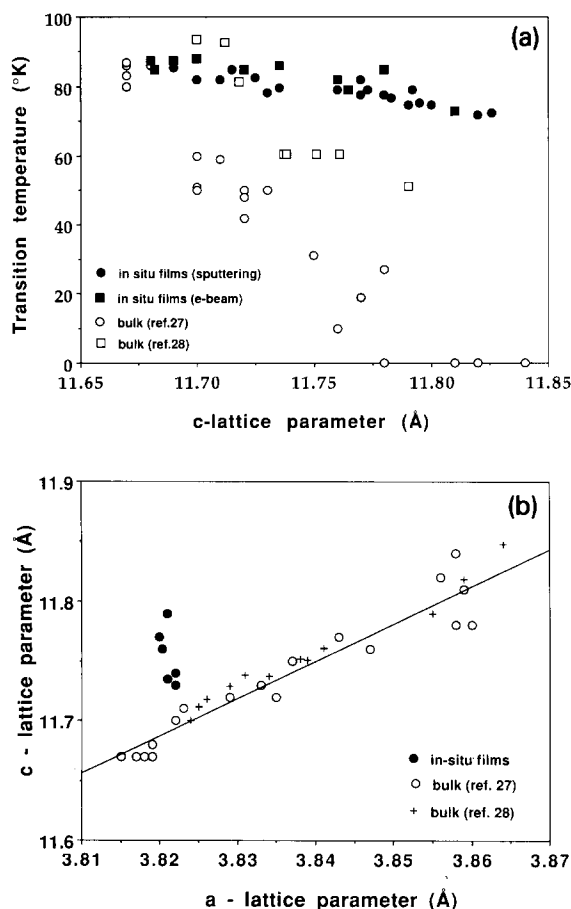


Fig. 7. (a) Transition temperature versus c -axis lattice parameter for in situ sputtered films (solid circles) and electron beam evaporated films [29] (solid squares) compared with those of bulk ceramics (open circles [27] and open squares [28]) (b) c -lattice parameter versus a -lattice parameter of thin films grown in situ compared to those of bulk ceramics [27,28].

Table II
Annealing experiment results of films grown in situ.

Substrate	Anneal condition	<i>c</i> -axis (Å)	<i>a</i> -axis (Å)	T_{c0} (K)
MgO(100)	650°C, 1 atm O ₂ , 3 h	11.75 to 11.75	3.82 to 3.82	81 to 81
SrTiO ₃ (100)	650°C, 1 atm O ₂ , 3 h	11.75 to 11.75	3.82 to 3.82	81 to 81
MgO(100)	850°C, 1 atm O ₂ , 1 h	11.75 to 11.70	3.82 to 3.82	81 to 85
SrTiO ₃ (100)	850°C, 1 atm O ₂ , 1 h	11.75 to 11.68	3.82 to 3.82	81 to 87
MgO(100)	400°C, 10mTorr O ₂ , 10 min	11.74 to 11.81	3.82 to 3.87	82 to 40
SrTiO ₃ (100)	400°C, 10mTorr O ₂ , 10 min	11.74 to 11.82	3.82 to 3.86	82 to 30
MgO(100)	400°C, 1 atm O ₂ , 10 min	11.81 to 11.73	3.87 to 3.82	40 to 82
SrTiO ₃ (100)	400°C, 1 atm O ₂ , 10 min	11.82 to 11.73	3.86 to 3.82	30 to 82

rameters to their original non-bulk values. Reversible entry and exit of oxygen in bulk material is well known to be caused by oxygen movement on the chain sites; the same apparently occurs in the in situ films.

3.4. Microstructures

Microstructural studies using transmission electron microscopy (TEM) have been carried out on films on SrTiO₃ (100) and MgO (100), with most work performed on those samples deposited on MgO. Because TEM provides only a two-dimensional projection of the microstructure, both plan-view and cross-sectional samples were examined whenever possible. Planar samples were prepared by cutting 3 mm disks from the 6 mm × 6 mm samples generally provided, mechanically thinning from the substrate side of the disk to a thickness of 100 μm and then dimpling to approximately 20 μm thickness. This was followed by argon ion milling at 5 kV and 0.3 mA, with the specimen holder attached to a cold finger immersed in liquid nitrogen. Cross-sectional specimens were prepared in a similar manner following standard procedures [31]. Care was taken to avoid exposure of the specimen to water at all stages of preparation. Samples were examined in a Philips EM 400 at 120 kV, or for high resolution studies in a Philips EM 430ST at 300 kV. Viewing normally was performed along one of the $\langle 100 \rangle$ zone axes of the substrate. The following is a brief overview of these studies; a more complete description will be given elsewhere [32].

As discussed earlier, three basic microstructures are found to occur on (001) oriented substrates: pre-

dominantly *a*-axis normal to the substrate (on SrTiO₃), mixed *a*+*c* normal to the substrate, and *c*-axis normal to the substrate. A high degree of in-plane and out-of-plane crystallographic alignment with the substrate is evident in all three cases, with the unit cell axes of the film aligned with those of the substrate. In addition, we often observe a second orientation variant on MgO, with the unit cell axes of the film aligned with the $\langle 110 \rangle$ of the substrate, a rotation of 45° from the first relationship as has been discussed by Ramesh et al. [33]; other orientation relationships demonstrated by them have been detected in our films by off-axis X-ray diffraction [34]. The size of these 45° rotated domains has been measured in one film, 123C4, to be of the order of 10 μm, and in another (63B5) to be of the order of 0.5 μm. They are thus seen to vary considerably in size. Given the large lattice mismatch between YBCO and MgO, it has been proposed by Tietz et al. [35] that the first orientation relationship is based on a matching of the oxygen sublattices in the MgO and YBCO.

Φ -axis scans of the YBCO (103) peak from two samples on MgO are shown in fig. 8. These represent two extreme conditions. Samples grown at 700°C show only a very small fraction of grains misoriented 45° in the plane. Samples grown at lower or higher temperatures contain 2–4% misoriented grains and misorientations at other distinct angles. Later in this paper, we discuss the relationship of these high-angle grain boundaries to high-frequency resistance losses.

A typical *c*-axis oriented region is seen in fig. 9 (sample 123A5). As expected, the film contains a high density of disordered, intersecting (110) twins with spacing in this specimen of 30 to 40 nm. It should be noted however that variation in the de-

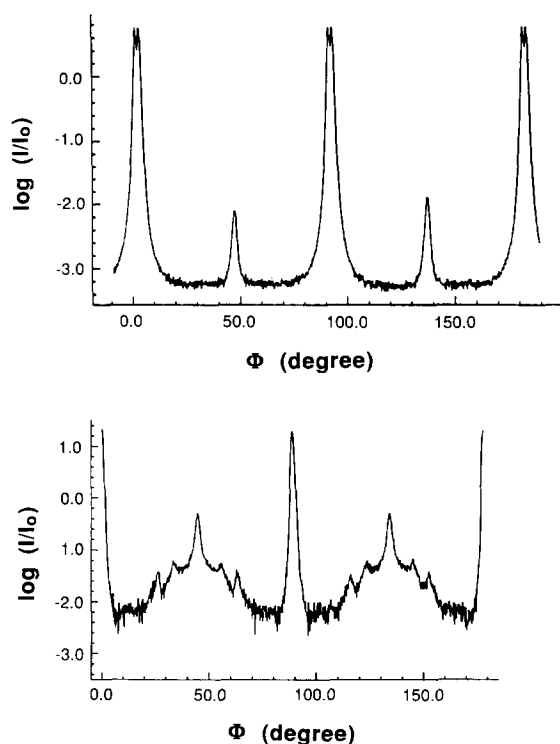


Fig. 8. Off-axis X-ray Φ scans of the YBCO (103) peak for the two films on MgO showing the effects of differing quantities of 45° misoriented grains. The splittings of the major peaks at 0 or 90° are due to saturation of the detector.

tailed structure of the twinning occurs with variation in the growth processing of the film, leading to twin spacings ranging from approximately 10 to 70 nm and twin lengths varying from 20 to 200 nm. More detailed investigations of the twinning process and morphology as a function of this processing are currently under way [36].

A low-magnification cross-sectional image, fig. 10, shows several features of the microstructure of a 150 nm thick, high critical current density film, 123B5, from the same deposition run as the above plan-view sample. First, this film is not truly a single crystal; interruptions in the structure are observable with spacings in the range of 100 to 200 nm. Second, the real surface (covered by the adhesive used in sample preparation) of the film is smooth and uniform except for an occasional a -axis grain (an example is marked "a" in the figure).

Figure 11 is a higher magnification image of the

same film near the substrate-film interface. This figure demonstrates that the boundary spacing in the near-substrate region appears to be smaller, about 50–70 nm, than that observed at low magnification. This may be explained by two phenomena. First, as Barry has pointed out [37], high resolution images in this $\langle 100 \rangle$ orientation are complicated by the fact that twin boundaries cut through the specimen at 45° along $\langle 110 \rangle$, giving rise to unavoidable tilts of about 1° between twin-related regions and leading to the overlap of [100]- and [010]-oriented YBCO. The twin spacing in this film is expected to be the same as that in fig. 9 (30–40 nm); certainly some of the boundaries visible in higher magnification phase contrast images such as this, but not in lower magnification diffraction/absorption contrast images, are twins. Second, it has been shown [38] that some YBCO defects have a tendency to "heal" as the film grows; thus we would expect some decrease in boundary density with distance from the interface.

In fig. 11 a grain misoriented from its neighbor by about 2° is visible, with the corresponding low-angle tilt boundaries marked by "A"s. This is a larger mosaic tilt than average for this film, as indicated by an X-ray rocking curve whose FWHM was 0.4° . At the right side of the picture is another boundary, marked with "B"s, this time with no measurable angular misorientation but whose contrast appears qualitatively different from that likely for a twin, as indicated by the few examples presented by Barry in the reference cited above. Also present are stacking faults along the c -axis, two of whose ends are labelled with arrows. Figure 10 also illustrates another feature of our films, namely that in general they display sharp film/substrate interfaces free of second phases.

On closer examination of fig. 11, the angular misorientation between the grains is seen to be caused by the fact that the film has grown with its c -axis normal to some averaging of the substrate surface normal and the substrate low-index crystallographic direction [001], not unreasonable given the 7–9% lattice mismatch between film and substrate. In this particular case, there is a slight slope of the substrate under the misoriented grain, leading to low-angle tilt boundaries between the regions with differences in their substrate surface normal. Thus it is demonstrated that substrate surface morphology can be a



Fig. 9. Microstructure of a *c*-axis YBCO film on MgO (film #123A5). A void, marked "V", near the center of the micrograph is an uncommon feature. Twin boundaries are visible as dark lines, with an example marked with "T"s.

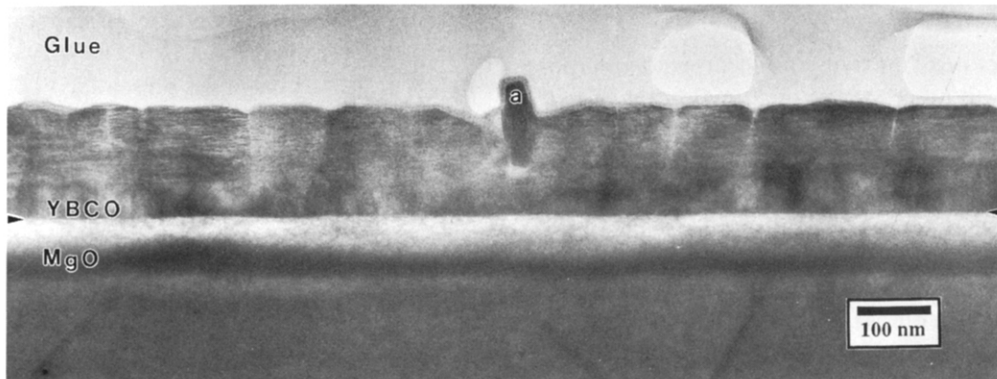


Fig. 10. Cross-section image of a 150 nm thick film on MgO, #123B5. The interface between the film and the substrate is marked with arrows. Glue used in sample preparation is visible above the natural surface of the film.

strongly contributing factor in the microstructure of these films.

The remains of an *a*-axis oriented grain (marked "a") is visible in the upper center of the film. It can

be seen that as the film has grown, the *a*-axis grain has enlarged laterally, forming a well-connected 45° grain boundary. This behavior is consistent with the observation that under some growth conditions,

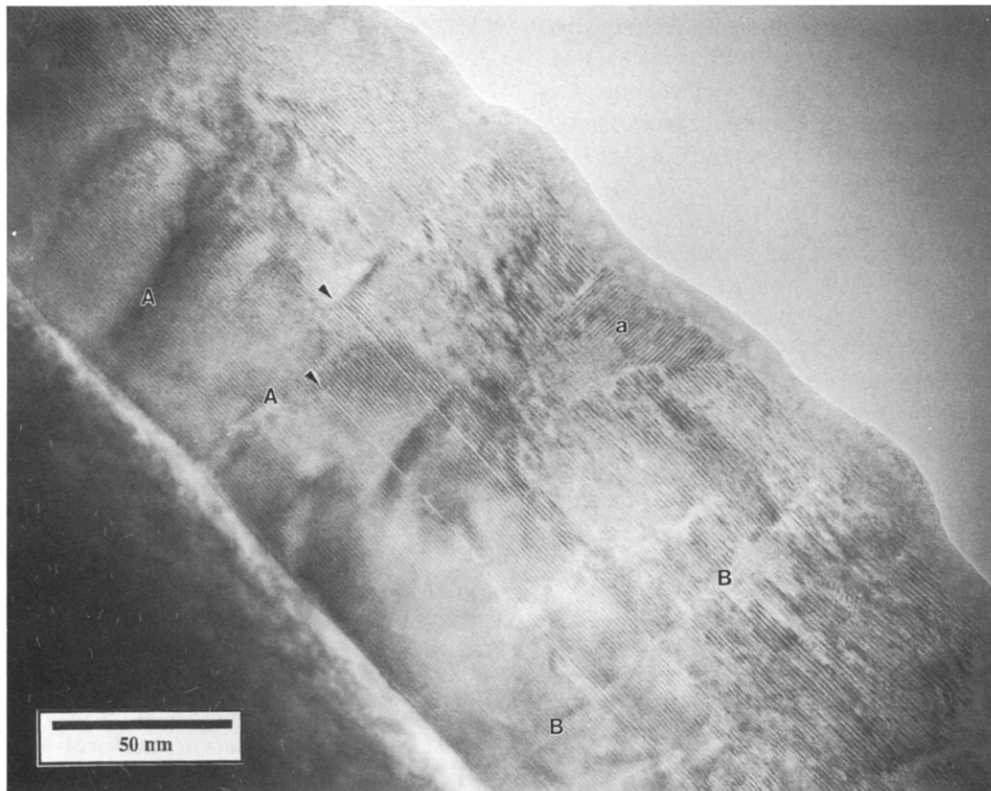


Fig. 11. Higher magnification cross-section image of 123B5. The 1.17 nm fringes of the c -axis are visible. The top of the film in this micrograph is not the true surface of the film but has been ionmilled during sample preparation; some ion-mill damage is also evident below the surface. Note the remains of an a -axis grain "a" and its connectivity with the c -axis matrix, and the boundaries marked by "A" and "B". Two stacking faults are indicated by arrows.

thicker films tend to have more a -axis oriented material (as measured by X-ray diffraction) than thinner films grown in the same manner.

3.5. Critical current densities

The current-carrying capability of our in situ grown films has been systematically studied. A typical value for this critical current density of c -axis oriented films is in the mid 10^7 A/cm² range at 4.2 K. This makes direct transport measurements difficult, so most of the J_c measurements were made using DC magnetization methods. These make use of the Bean formula, which for our thin film geometry can be readily applied. The agreement between J_c values derived

from magnetization and transport measurements has been verified by direct comparison.

3.5.1. Magnetic measurements

Critical currents for H parallel to the c -axis direction (perpendicular to the film surface) were studied as a function of temperature and applied field by measuring the induced saturation moment on a Princeton Applied Research 155 vibrating sample magnetometer, in conjunction with a Varian magnet capable of generating a field of up to 18 kG. The DC moment was measured by ramping the field to a certain value, allowing the moment to decay for ~ 1 s, and then measuring the sample moment. The Bean formula [39]

$$J_c(H) = \frac{30m(H)}{VR} \quad (1)$$

was applied to relate the observed hysteretic moment $m(H)$ to the critical current $J_c(H)$ at each applied field value, where V is the film volume. R is chosen as the geometrically averaged sample radius. A typical magnetization loop obtained in this fashion is shown in fig. 12.

3.5.1.1.

Temperature dependence of the critical current. Magnetization hysteresis loops were measured for several films at various temperatures between 4.2 and 81 K, in the field range from -15 kG to 15 kG. The observed moment reached a maximum near zero applied field and was found to decrease monotonically with the absolute value of the applied field, as illustrated by fig. 12. Even in this relatively limited magnetic field range ($H \ll H_{c2}$), it was found that critical currents were significantly affected by the applied field.

Figure 13 shows the critical current as a function of temperature as determined from the Bean formula at three applied fields. (0 kG, 5 kG, and 10 kG) for a 3000 \AA film on MgO. Values obtained for zero applied field are affected by self-field effects, as will be discussed in the Appendix. Model calculations assuming the Kim expression [40] for the field dependence indicate that the impact on the observed critical current from these effects are usually small, less than 10% of the calculated J_c value for typical parameters. For instance, for $H_0 = 10$ kG, $J_c(H=0) = 3 \times 10^7 \text{ A/cm}^2$, and $l = 3000 \text{ \AA}$, it was found that currents at zero applied field were re-

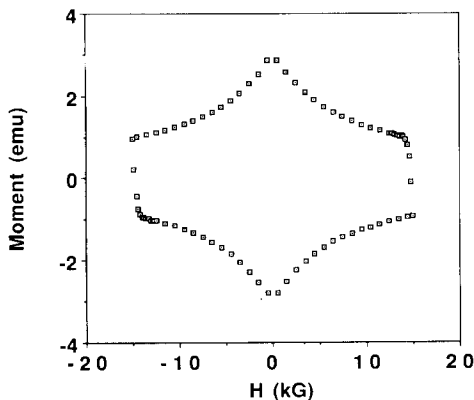


Fig. 12. Typical magnetization loop at 4.2 K for 3000 \AA YBCO film deposited on MgO.

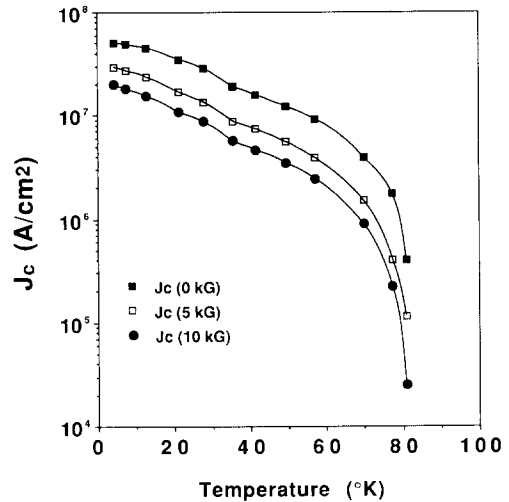


Fig. 13. Critical current density vs. temperature for a YBCO film on MgO at different values of applied field.

duced by 6% by the self field. The Bean model we use will underestimate J_c at zero applied field in samples for which the Kim model is applicable.

The temperature dependence of J_c illustrated in fig. 13 is similar to that reported by others for thin films [41] and single crystals of 1-2-3 compounds, showing an exponential dependence of critical current on temperature for temperatures less than approximately 50 K [42,43]. At higher temperatures, a linear relationship between J_c and $(T - T_c)$ is observed. This type of linear behavior has been interpreted in terms of weak link coupling, e.g. Josephson tunnelling, in ceramics and in post-annealed films.

Critical currents for our sputtered films determined from magnetization measurements are quite high. The film in fig. 13, which has a critical temperature $T_{c0} = 86$ K, has a critical current of $5 \times 10^7 \text{ A/cm}^2$ at 4.2 K and $2.5 \times 10^6 \text{ A/cm}^2$ at 77 K. This indicates that the flux vortex pinning is very strong in these films, approaching the theoretical core pinning force derived from Ginzburg-Landau theory [44]. Thus the flux vortices must be pinned along a substantial fraction of their length in these thin films, either by a large density of point defects [44] or along surfaces.

3.5.1.2.

Field dependence of the critical current. The field dependence of J_c we observe below 15 kG for sputtered

thin films is typically weaker than has been observed for bulk ceramic samples [45], in situ laser ablated films [46], and post-annealed films [47]. The observed field dependence is comparable to results obtained on single crystals [48], but the observed current densities in our films are approximately an order of magnitude higher. The latter result shows that intrinsic pinning can play only a minor role.

Hysteresis loops at high temperature (> 77 K) exhibited reversible magnetization near the top of the field scan range, above a temperature dependent irreversibility field H_{irr} . For magnetization data presented here, the maximum applied field was always less than H_{irr} , except for $T > 77$ K. For fields $H < 0.5H_{\text{irr}}$, it was observed empirically that $J_c(H, T)$ could be described for many films by the phenomenological Kim expression [40]

$$J_c(H, T) = \frac{J_c(0, T)}{1 + (H/H_0)} \quad (2)$$

for temperatures less than 77 K and applied fields less than 15 kG. This functional form was found to yield better fits to our data than did other functional forms which have been used in this field range [41]. In this region eq. (2) provides a straightforward way to compare the field dependence of J_c for different samples.

The interpretation of the parameters $J_c(0, T)$ and H_0 are model dependent. In a flux pinning model, in the absence of flux creep, $J_c(0, T)$ is a measure of the maximum pinning force exerted on an isolated flux vortex before depinning occurs, while the field dependence is determined by the superconducting properties, e.g. H_{c2} , or by the pinning microstructure [49]. The functional dependence in eq. (2) is often observed for thin film superconductors [50]. Near the irreversibility point H_{irr} or near H_{c2} , eq. (2) is inadequate for describing the critical current, since it does not yield a volume pinning force which decreases with increasing field. Magnetization measurements to 10 T made on some samples do in fact show departures from eq. (2) at high applied fields, even at low temperature. Except at high temperatures (> 77 K) our measured field range is much less than either H_{irr} or H_{c2} .

Typical values for H_0 for our films were found to lie between 2 and 20 kG, depending on temperature and film processing conditions. Values for $J_c(0, T)$

were also found to depend on deposition parameters, but both the critical current at 4.2 K and H_0 were repeatable for a given set of processing conditions. Figure 14 illustrates fits of (2) to a 4000 Å YBCO film on a polished single crystal MgO substrate, at three different temperatures. As can be seen in the figure, a reasonable fit is obtained.

Equation (2) can be used to phenomenologically specify $J_c(H, T)$ over the entire temperature and field range measured by specifying $J_c(0, T)$ and H_0 versus temperature. This is done in figs. 13 and 15 for the 3000 Å film on MgO. H_0 is obtained by a least squares fit of magnetization data between 1.0 kG and 10 kG.

It was found that the field dependence of the critical current could be systematically altered by changes in deposition conditions. Figure 16 illustrates these changes in field dependence in the range $0 < H < 15$ kG, with $J_c(H, T)$ normalized to $J_c(0, T)$. Curve (a) is for a 2000 Å film on a LaAlO_3 (100) substrate, deposited with $P_{\text{O}_2} = 60$ mTorr, $P_{\text{Ar}} = 40$ mTorr, at a temperature of 680°C. This film has a critical current of 2×10^7 A/cm² measured at 4.2 K. The solid line is a fit of form (2), with $H_0 = 24$ kG. Curve (b) is for a 3000 Å film deposited on MgO with $P_{\text{O}_2} = 10$ mTorr, $P_{\text{Ar}} = 40$ mTorr, at a temperature of 640°C. This film has a critical current at 4.2 K, in zero ap-

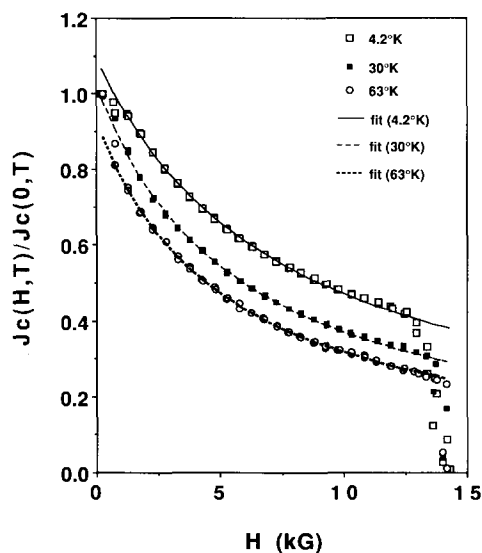


Fig. 14. Fits of the form eq. (2) for three temperatures (4.2 K, 30 K and 63 K).

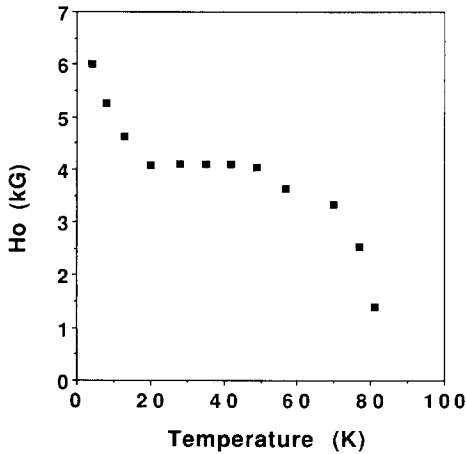


Fig. 15. Least square fit values for H_0 vs. temperature.

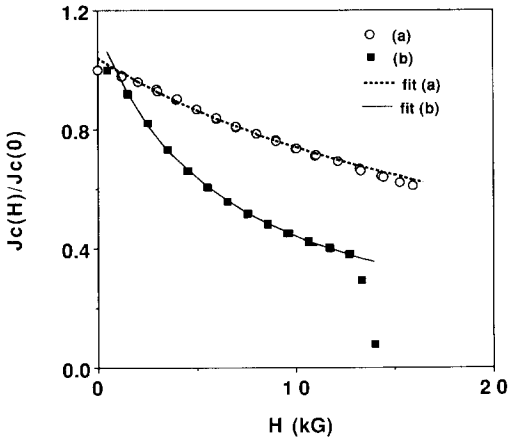


Fig. 16. Different field dependence for two different samples (a) YBCO on $LaAlO_3$ (912C6) and (b) YBCO on MgO (182B4) measured at 4.2 K. Lines are fits of the form of eq. (2).

plied field, of 5×10^7 A/cm². The solid line is a fit of the form (2) with $H_0 = 6.2$ kG.

Certain aspects of the magnetization data support the belief that weak links may be present in these thin films. The temperature dependence of H_0 shown in fig. 15 is qualitatively similar to the scaling field H_0 defined in ref. [51] for bulk ceramic samples, in which weak link behavior is believed to dominate the critical current. Cross-sectional TEM micrographs support the existence of possible weak link structures in these films, especially near the substrate. Stacking faults, antiphase boundaries, and low

angle tilt boundaries are all observed to be present in the films. Mannhart et al. [52] demonstrated that weak link behavior is observable for tilt boundary angles as small as 5° . Also, the observed temperature dependence of H_0 is weak at temperatures below ~ 70 K, which is consistent with the critical current being limited by geometric factors, rather than by the strength of the fundamental vortex interaction energy. For critical currents limited by homogeneous pinning, the scaling field H_0 would be expected to scale with H_{c2} [53]. The linear temperature dependence of the critical current near T_c , and the field dependence in these thin films, as well as the magnitude of J_c , are qualitatively similar to the behavior observed in granular NbN thin films, in which weak links are believed to control the critical current [54,55]. It is therefore plausible that these films possess some granularity which affect the critical current in relatively low magnetic fields ($H \ll H_{c2}$). Under some conditions, in high field weak links might be pinning sites [56].

Other mechanisms for the limitation of the observed critical currents, such as depairing, flux creep, and pinning by point defects, provide less satisfactory agreement with the above observations. Ginsburg–Landau theory predicts for zero magnetic field $J_c \propto (T_c - T)^{3/2}$ near T_c , for depairing [57], rather than the observed $(T_c - T)$ dependence over a relatively wide temperature range (50–80 K).

It has been suggested that observed the field dependence of J_c may be due to flux creep, [58] through the relation

$$J_c(H, T) = J_{c0} \left[1 - \frac{kT}{U_0} \ln \left(\frac{Bd\Omega}{E_c} \right) \right], \quad (3)$$

where d is the characteristic hopping distance, Ω is the flux bundle attempt frequency, and E_c is the electric field imposed by the applied magnetic field ramp. The critical current in this expression depends implicitly on magnetic field through the activation energy U_0 . U_0 is expected to decrease monotonically with increasing temperature, perhaps as $(T_c - T)^{3/2}$ (see for example ref. [58]). This would predict that the characteristic field dependence, which we characterize by H_0 , would scale strongly with temperature. This is not consistent with the observed H_0 , being roughly constant with temperature. It should

be noted that many different models for flux creep in high- T_c superconductors exist, [59,60] some of which may be capable of yielding the observed magnetization versus field behavior.

Changes in the field dependence of J_c , or the volume pinning function $J_c \times B$, are the result of changes in either the pinning or weak link microstructure, or in the superconducting properties of the film. Two readily identifiable defects in thin films, which might be considered as candidates for pinning sites, are twin boundaries and point defects. Experiments have shown that the twinning microstructure does not significantly affect the observed critical current or field dependence in these thin films [61]. Point defects, in the form of site substitutions and oxygen vacancies, might be expected to occur with very high densities for films grown at low temperatures. However, it is not clear that a simple change in the pinning site density, in the case of a very dense array of pins, will affect the field dependence of J_c . For dense arrays of defects, experiments on superconducting niobium [62] demonstrated that the field dependence of J_c at high fields was unaffected by the density of pinning sites. Collective pinning theory also yields this same conclusion [63]. Positive identification of the pinning sites and mechanisms in these thin films will require the preparation of samples of known defect structure and measurements at higher fields.

3.5.2. Transport measurements

DC transport J_c was measured on patterned films. The critical current for a 250 μm wide wet-etched film exceeded the limit of the measurement capacity of our present setup ($1 \times 10^5 \text{ A/cm}^2$), at 1.5 K below T_{c0} . In an investigation of edge pinning the J_c of an ion-milled 1 μm -wide-bridge on MgO at 4.2 K was found to be $2 \times 10^7 \text{ A/cm}^2$. However, the T_c of that film was degraded by 10 K during the ion-milling process for reasons that are not intrinsic since no degradation was observed on laser ablated films on SrTiO_3 . Figure 17 is a J_c versus temperature curve of a 1 μm -wide bridge measured by transport [64]. The J_c is in good agreement with the magnetization measurement ($2 \times 10^7 \text{ A/cm}^2$ at 4.2 K and at zero field) made prior to the patterning in spite of the degradation of T_c .

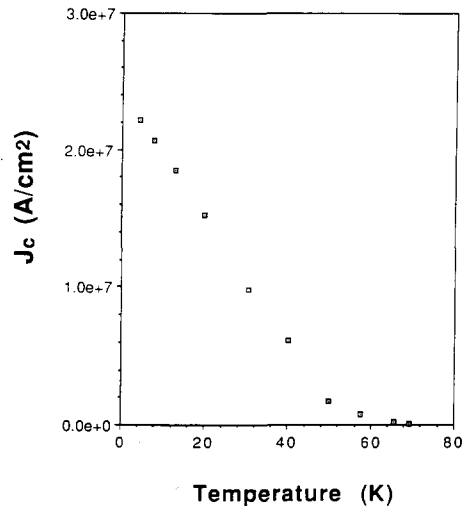


Fig. 17. J_c vs. temperature curve of YBCO thin film on MgO substrate measured by transport.

3.6. Transport properties in a magnetic field and decay of magnetic shielding current

To investigate the dissipation related to the motion of magnetic vortices, we have measured transport properties in a magnetic field [65]. Two 4000 \AA thick films on MgO (100) substrates were patterned into 250 μm wide, 2 mm long bridges using wet chemical etching. There was no degradation of T_c and resistivity of these films after the patterning process. A four-point measurement was then made with the sample placed in a superconducting magnet. The measurement current density was 200 A/cm^2 .

Three different directions of the magnetic field with respect to the sample and the current were studied: $H \perp J$ and \perp to the a - b plane, $H \perp J$ and \parallel to the a - b plane, and $H \parallel J$ and \parallel to the a - b plane. In all three cases, $J \parallel$ to the a - b plane. Figure 18 shows the resistive transition broadening for these three configurations as a function of magnetic field. In all three, the transition width increases with increasing magnetic field. The amount of broadening is different for each configuration. Even so, the broadening is most significant when the magnetic field is perpendicular to the a - b plane. The broadening is less than has been observed in some post-annealed films [66] and single crystals [67]. Figure 18(b) shows data for the magnetic field parallel to the Cu-O planes while the

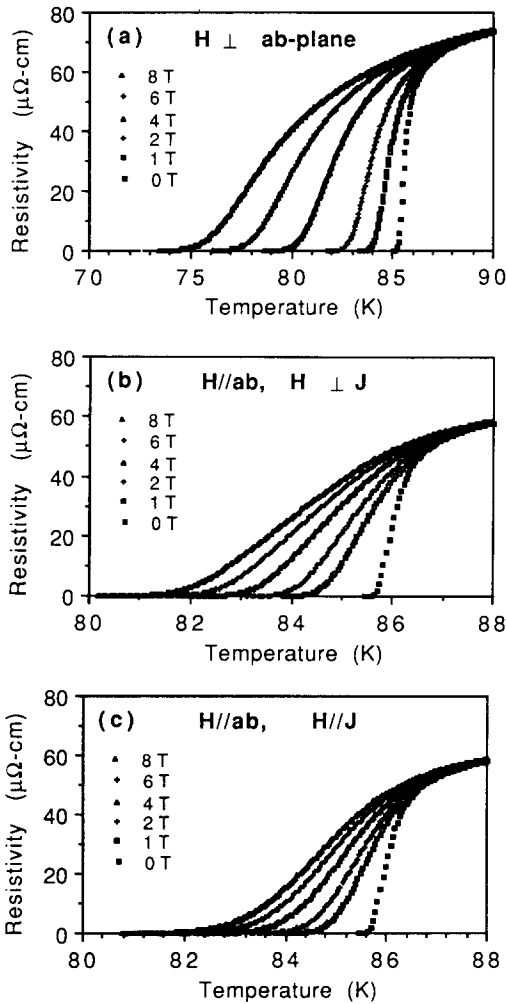


Fig. 18. Resistive transition broadening of YBCO thin films on MgO for various configurations as a function of magnetic field. (a) $H \perp a$ - b plane and $H \perp J$, (b) $H // a$ - b plane and $H \perp J$, (c) $H // a$ - b plane and $H // J$.

current remains perpendicular to the field. The broadening of the transition in this case is much less than shown in fig. 18(a), which could imply that vortices trying to hop across the Cu-O planes experience much stronger pinning than vortices moving in the Cu-O planes. This is consistent with the calculation of Tachiki and Takahashi [68] based on a strong modulation of the superconducting order parameter along the c -axis. In the configuration used for obtaining the data in fig. 18(c), the applied field and the net current are in the same direction. If the

local currents were always parallel to the net macroscopic current, there would be no Lorentz force on the vortices. The reduction in broadening accompanying this rotation of the magnetic field in the a - b plane demonstrates that in these films a considerable portion of the broadening seen with $H \perp J$ is due to Lorentz force assisted flux motion. The origin of the broadening seen with $H // J$ is, at this stage of analysis, uncertain. Such broadening may be a consequence of bent microscopic current paths resulting from the grain structures. Weak links can also contribute to a broadening that is relatively insensitive to the orientation of the field. Further analysis of the data is underway to elucidate the origin of this broadening.

Due to the motion of magnetic vortices, these in situ grown YBCO films, like most type-II superconductors, exhibit dissipation in the presence of a magnetic field. Such dissipation demonstrates itself both as a broadened J - E characteristic and as a finite relaxation of the magnetic shielding current. A simple relation has been established between the local J - E characteristic and the relaxation of the magnetic shielding currents [69]. Our experimental results indicate that such relaxation remains insensitive to temperature over a wide range from 60 K down to 10 or 20 K, making simple thermally activated vortex creep motion an unlikely explanation.

The J - E characteristic can be most directly observed by making transport measurements on patterned films in a magnetic field. Figure 19 summarizes the result. The apparent linearity of the plot on

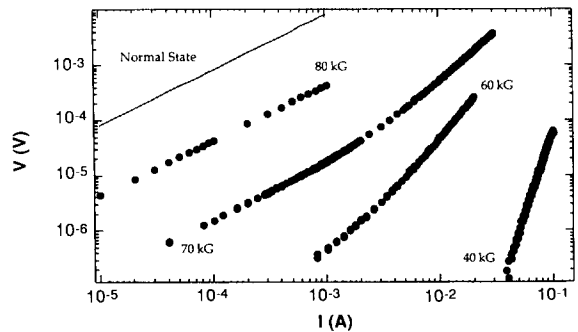


Fig. 19. J - E characteristic measured on an in situ YBCO thin film on MgO (191B4) with field perpendicular to the a - b plane (after ref. [64]).

the log-log scale suggests that the J - E characteristics are power-law in nature and do not follow from the simple exponential behavior which would be expected were the loss determined by vortex creep, although at the high field limit (80 kG, 73 K) an ohmic J - E characteristic does seem to emerge. This could be due to the viscous flow of the vortices after being completely de-pinned. A simple cross-over between the vortex creep and vortex flow region, as worked out by Sun, et al. [69], is insufficient to account for the power law type of behavior extending over three to four decades in voltage. Due to the limitation of the measurement current, transport measurements cannot be extended far below T_c . The relaxation of magnetic shielding current is therefore considered as an alternative to obtain dissipation information over the entire temperature range.

Magnetic relaxation studies are performed by monitoring the decay of the magnetic moment induced by the magnetic shielding current inside the film. Fields up to 18 kG are applied perpendicular to the unpatterned film. The magnetic moment relates to the shielding current through the Bean formula as long as the current distribution remains in the "critical state", which is the case here. One set of such relaxation data as a function of temperature is shown in fig. 20, in which the magnetic moments

have been normalized to their initial value for clarity. A large residual relaxation seems to persist to very low temperatures, without the trend of extrapolating back to zero as the temperature is cooled far below T_c . This is unexpected from simple thermal activation models. It is, however, not inconsistent with the possibility of a power law J - E characteristic in the low temperature limit. It has been shown [69] that a power law J - E characteristic

$$E = \alpha J^n \tag{4}$$

will result in a magnetic shielding current relaxation with a characteristic time dependence of

$$M(t) = M(0) \left[1 - \frac{1}{n} \ln \left(\frac{t}{\tau_1 + 1} \right) \right] \tag{5}$$

if $n \gg 1$, where n is the power law exponent, and time, t is small enough so that

$$M(0) - M(t) \ll M(0) . \tag{6}$$

Figure 21 plots the n derived from the data as a function temperature from both magnetic measurements and transport measurements. Although parameters of the measurement do not overlap, a clear trend exists and it is continuous from the magnetically obtained exponent to the transport measured

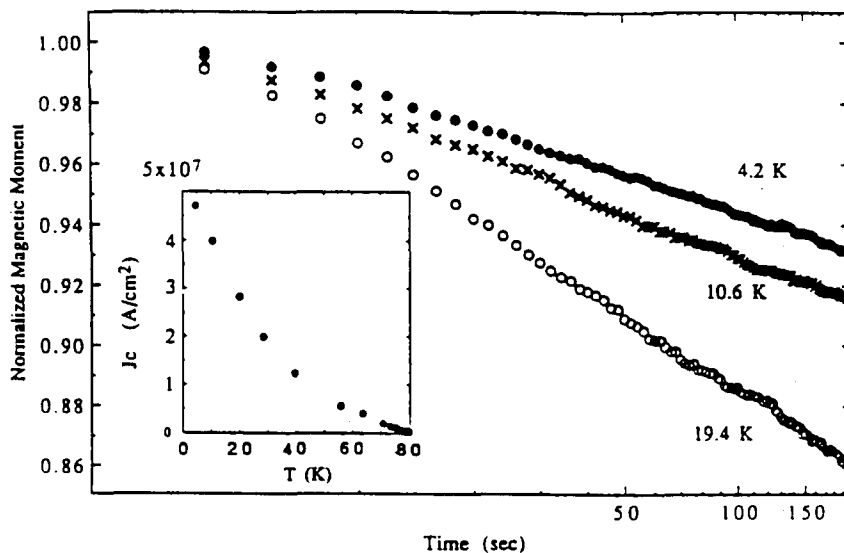


Fig. 20. The relaxation of the magnetic shielding moment at different temperatures.

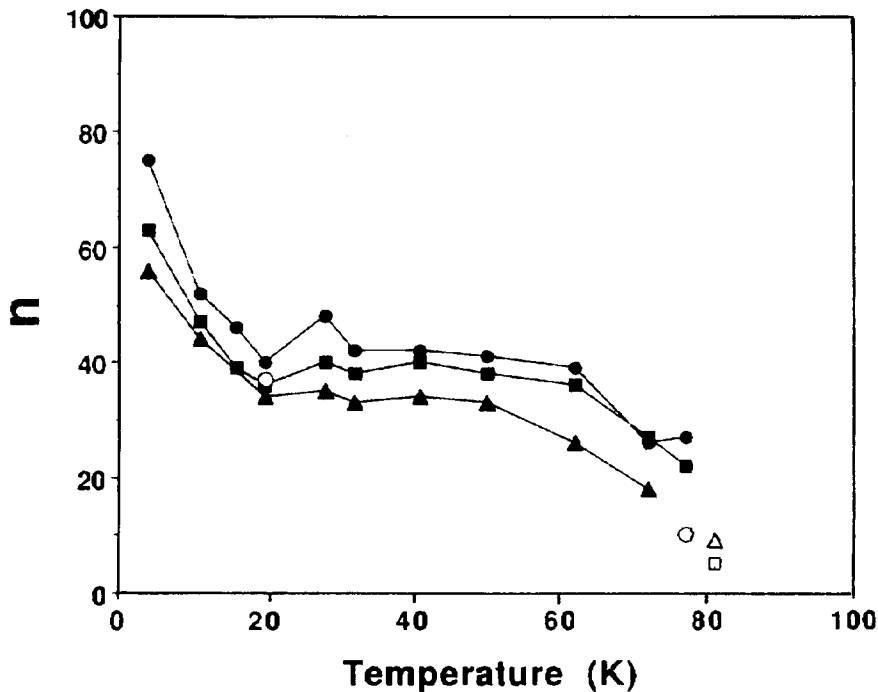


Fig. 21. Power law exponent as a function of temperature from both magnetic measurements and transport measurements (after ref. [64]). (●) magnetic (5 kG), (■) magnetic (6 kG), (▲) magnetic (9 kG), (○) transport (0 kG), (□) transport (5 kG) and (△) transport (10 kG).

exponent, supporting the relation we found between the local $J-E$ characteristic and the decay of the magnetic shielding currents.

Power law shaped $J-E$ characteristics have long been observed in conventional type-II superconductors and have been considered in general to be the consequence of a spatial variation of the local critical current density throughout the sample [69]. Table III lists the power law exponents for some other type-II superconductors. As can be seen from the table, a power law exponent of 40 such as those of our YBCO films is really not that different from several rela-

tively well known conventional type-II superconductors. A detailed calculation by Hampshire and Jones [70] indicates that such a power law exponent will correspond to a critical current distribution $\langle J_c(r) \rangle$ of only 16% over the entire body of the sample – a distribution that is certainly possible considering the abundance of stacking faults and various boundaries that can cause inhomogeneous current flow.

To conclude, a power law $J-E$ characteristic was observed in our in situ grown YBCO thin films, the exponent is rather temperature insensitive and remains around 40 to 60 in the entire temperature range except when very close to T_c or below 10 K. This behavior can be attributed to the existence of a small variation of the critical current density throughout the sample. The exact origin of such inhomogeneity is now under further investigation.

Table III
Power law exponents for some type-II superconductors.

Material	Power law exponent	Refs.
Nb_3Sn wires	2 to 14	[70]
Nb_3Sn wires	5 to 70	[71]
V_3Si sintered	50 (4 kG), 97 (6 kG)	[72]
V_3Si arc melted	102 (6 kG)	[73]
NbTi filaments	30 to 150	[74]

3.7. RF properties

3.7.1. Surface resistance

The purity, high degree of epitaxial alignment, clean grain boundaries and surface smoothness of the in situ films discussed here make them attractive candidates for use at microwave frequencies in low loss applications. Microwave studies of these films may indicate the electrical nature of other remaining defects, and intrinsic loss mechanisms. As has been made clear above, the in situ films are physically distinct from post deposition annealed materials and equilibrium single crystals. It is interesting, then, to see how the microwave properties compare.

Resistive losses were measured at 4.2 K near 10 GHz for 13 films and as function of temperature for three pairs of films. The measurements were performed using a parallel plate resonator technique [76]. In this method, two square $1\text{ cm} \times 1\text{ cm}$ samples of superconductor are pressed face to face with a thin dielectric placed between them. This configuration provides a family of transverse electromagnetic modes. The bandwidths of these modes can be used to calculate the average surface resistance of the two superconducting materials in a straightforward fashion. When this apparatus is used to measure thin films of Nb, a value of $24\ \mu\Omega$ is obtained at 11 GHz and 4.2 K. This value is consistent with cavity based measurements of solid Nb at 4.2 K [77].

Table IV shows the results of surface resistance

measurements at 4.2 K. Film thicknesses varied from 3000 to 5000 Å. Even without microcracks or other possible sources of leakage, taking the penetration depth to be about 1400 Å [78], we expect power lost through the sample to contribute to the measured bandwidth. The data reported here have not been corrected for such effects. The lowest values ($16\ \mu\Omega$ at 4.2 K and 10 GHz) reported in table IV are the lowest that have been reported to date for YBCO, consistent with the film quality described above but orders of magnitude greater than expected for an ideal superconductor with an isotropic BCS energy gap.

A wide variation in the loss at 4.2 K, is apparent. Conditions are indicated in table IV which reproducibly result in 4.2 K loss at 10 GHz near $25\ \mu\Omega$ or less. We have studied the relationship of these values to other physical parameters as will be reported in detail separately [79].

The results can be summarized as follows. The higher losses can be quantitatively accounted for by the presence of high angle grain boundaries associated with X-ray intensities at $\Phi=45^\circ$. Figure 22 shows the relation between R_s and the quantity of misaligned material. The line passes through the data for the two highest loss samples within experimental error. We conclude that overall there is a clear correlation between the volume fraction of *c*-axis oriented material misaligned at high angles in the surface plane and the values of R_s . The higher loss samples are dominated by losses associated with the

Table IV
Surface resistances of various films at 4.2 K and 10 GHz.

Sample #	R_s at 4.2 K, 10 GHz ($\mu\Omega$)	Substrate	T_{sub} ($^\circ\text{C}$)	$I(45^\circ)/I(0)$ ($\times 10^2$)	$\rho(0)$ $\mu\Omega\text{cm}$	T_c (K)	ΔT_c (K)
M058C56	16	MgO	700	0.026	22	84.5	1
M058D56	23	MgO	700	0.129	35	83	1
M058D45	25	MgO	700	0.031	21	84.5	1.5
M058C45	26	MgO	700	0.093	–	84.5	1
203B34	38	MgO	650	0.122	45	78	2
L026B45	42	MgO	700	0.127	39	82	1
203C34	64	MgO	650	0.136	60	72	3
214B34	108	MgO	650	0.225	60	75	3
M082B45	545	MgO	720	3800	–	85	1
214C34	744	MgO	650	3500	60	73	3
L027B45	> 1 m Ω	MgO	760	–	–	–	–
L024C45	40	LaAlO ₃	730	–	–	–	–
L027C45	32	LaAlO ₃	760	–	–	–	–

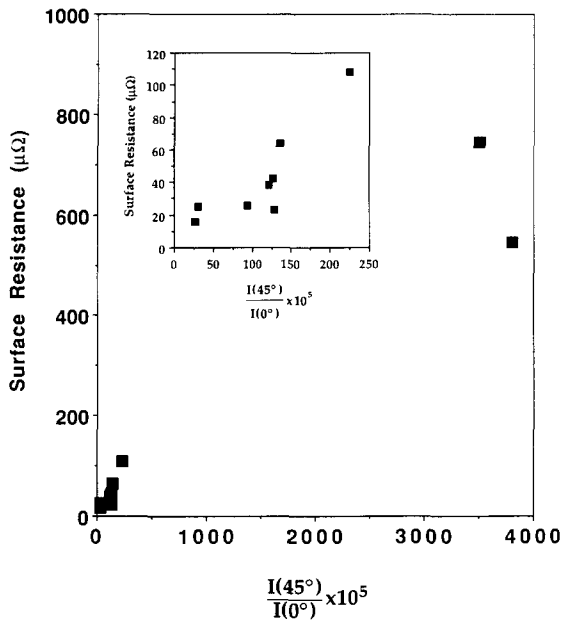


Fig. 22. The relationship between R_s at 4.2 K, 10 GHz and fraction of 45° misalignment grains in the YBCO films on MgO. Inset shows the lower loss regime.

boundaries between aligned and misaligned material and the losses in most of the samples have at least a considerable component due to the same features. For the films in the lower loss regime, we still find a weak correlation to the volume fraction of high angle grain boundaries. The scatter at the lower loss end of the plot suggests that either the influence of the misaligned material varies amongst the samples or that another variable loss mechanism is being observed in this regime. However, there was no clear correlation between R_s and rocking curve width, amount of a -axis material, or the presence of impurity elements.

At temperatures above or below what we have found is optimum for growth ($650\text{--}700^\circ\text{C}$), many 45° grains can be found in the films deposited on MgO substrates. (See table IV) Growth of YBCO films on LaAlO_3 substrates does not as readily lead to 45° grains because the lattice match is good, and they have the same perovskite structure. Films grown at the high temperature on MgO and LaAlO_3 show very different behavior. In contrast to a film deposited on MgO, films grown on LaAlO_3 exhibit R_s val-

ues comparable to the best films on MgO even when the substrate temperature is increased to 760°C . Films grown at high temperature on LaAlO_3 by Newman et al. [18] also using a 90° off-axis sputtering system have lower R_s at high temperature (at 77 K) even when residual losses at low temperature (4.2 K) are slightly higher. Confirming data are given in table IV. Figure 23 shows the temperature dependence of R_s , showing different behavior in the high temperature region for films grown on MgO and LaAlO_3 .

We have also investigated some relations between R_s and normal state properties and DC superconducting properties such as resistivity, $\rho(0)$ and critical current. There is a strong correlation between R_s and the normal state resistivity. The normal state resistivities plotted as a function of temperature for films grown on MgO have nearly the same slope but varying extrapolated-to-zero temperature intercepts. The relationship between R_s and $\rho(0)$ is shown in fig. 24. Note that unlike the correlation displayed in figure 22 the trends in fig. 24 appear to extrapolate to R_s values significantly lower than the lowest observed value. Note also that the apparently linear trend in the lower loss samples does not extrapolate at all well to the R_s values observed for the two highest loss films for which $\rho(0)$ is known. These intercepts correlate to T_c , increasing as T_c falls. While it has not yet been possible to interpret these trends uniquely, they may suggest that deposition param-

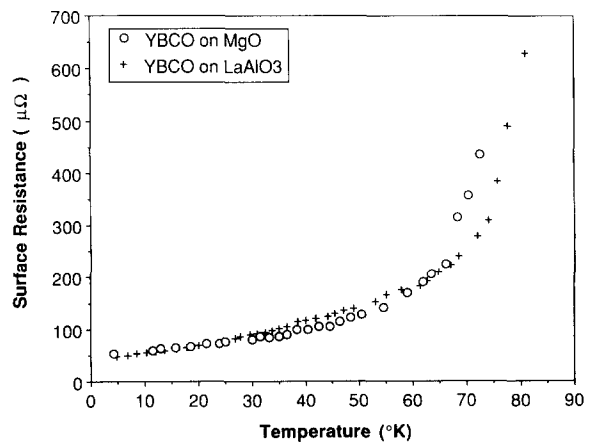


Fig. 23. R_s vs. temperature curves of a pair of YBCO thin films on MgO (\circ) and LaAlO_3 ($+$): Newman, et al. [18].

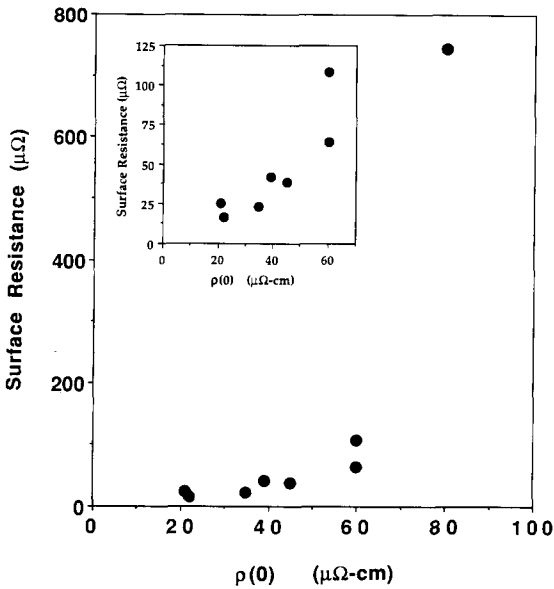


Fig. 24. The relationship between R_s at 4.2 K, 10 GHz and $\rho(0)$ of the YBCO thin films on MgO. Inset shows the lower loss regime.

eters consistent with a very high degree of epitaxial order have some residual local disorder. The residual disorder could increase the normal carrier scattering rate as well as the residual losses at 10 GHz in the superconducting state. A more complete discussion appears elsewhere [79].

The dependence of the 10 GHz resistivity as a function of temperature for a closely matched pair of films is shown in fig. 23. The values near $T_c = 85$ K are close to those expected for a simple two fluid model using BCS-like behavior and reasonable parameters for YBCO. The values below $0.7T_c$ deviate considerably from such a model and these deviations appear to be poorly described by a BCS-like function plus a temperature independent constant. The origin of this high, temperature dependent loss at low temperatures is currently under investigation.

3.7.2. Penetration depth

The value of the magnetic penetration depth λ at zero temperature is one of the fundamental length scales in superconductivity. The penetration depth is also important for understanding the RF surface resistance since it determines the volume of interaction between the RF field and the material. We have

measured the penetration depth of the in situ films on various substrates and with different textures. Measurement of the magnetic penetration depth is achieved by measuring the characteristics of a superconducting transmission line resonator made with the thin films operating at microwave frequencies [80,81].

Measurements of the magnetic penetration depth involve both the temperature dependence and magnitude of λ . Determining the absolute magnitude is considerably more difficult, and less exact, than measuring the temperature dependence of λ in the transmission line resonator technique. The temperature dependence of $\lambda(T)$ for $T < T_c/2$ can be determined directly from the data in the microstrip resonator technique [82]. Figure 25 is a plot of the raw data in a form which is proportional to $\ln((\lambda(T)/\lambda(0)) - 1)$ in the limit $T < T_c/2$ [82]. In fig. 25(a), representative data are plotted against T_c/T (normalized at $T_c/T=2$) in the expectation that the penetration depth temperature dependence is activated over an energy gap $2\Delta(0)$,

$$\frac{\lambda(T)}{\lambda(0)} - 1 \propto \exp(-\Delta(0)/k_B T), \quad T < T_c/2. \quad (7)$$

The in situ sputtered films have similar temperature dependencies for $\lambda(T)$, but no single exponent characterizes their temperature dependence. $\text{YBa}_2\text{Cu}_3\text{O}_7$ films prepared by other techniques (e.g. in situ evaporation and laser ablation) as well as films prepared by in situ sputtering in other chambers show significantly different temperature dependencies and values for $2\Delta(0)/k_B T_c$ in the range 0.9 to 2.2 [82,83]. However, films grown on the same substrate tend to cluster together on this plot. In general, films grown on MgO show higher values for the slope ($2\Delta(0)/k_B T_c$) than those grown on LaAlO_3 or yttria stabilized zirconia [83,84]. In fig. 25(b) the same data are plotted against $\ln(T/T_c)$ in the expectation that the penetration depth temperature dependence is polynomial,

$$\frac{\lambda(T)}{\lambda(0)} - 1 \propto \left(\frac{T}{T_c}\right)^n, \quad T < T_c/2. \quad (8)$$

Once, again, the in situ sputtered films show similar values for the exponent n ($n=2.5$), but $\text{YBa}_2\text{Cu}_3\text{O}_7$ films prepared by other techniques and on other sub-

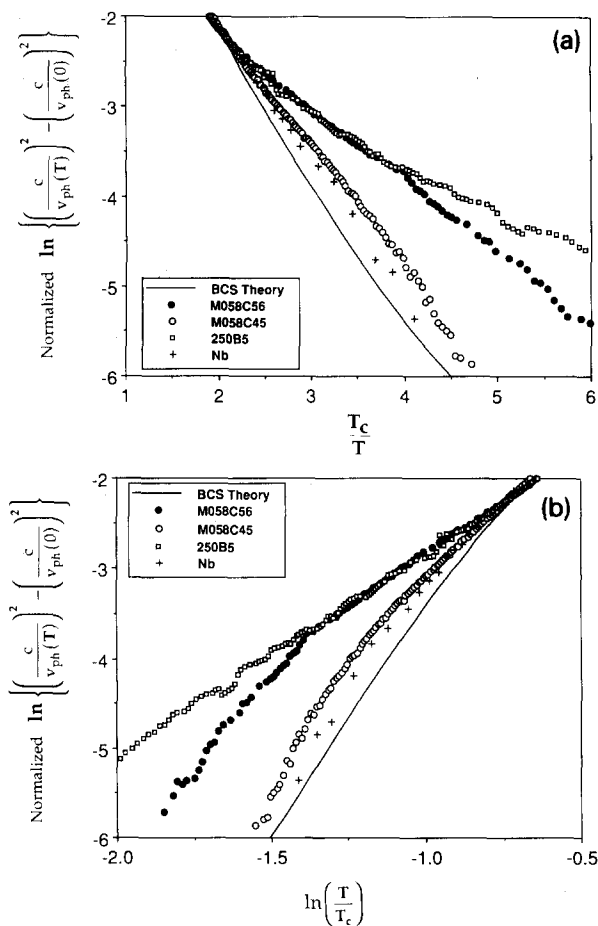


Fig. 25. (a) Plot of measured phase velocity data vs. T_c/T , normalized at $T_c/2$, for Nb (+), in situ YBCO films on MgO (solid and open circles) and LaAlO_3 (square), and BCS theory (line). (b) Plot of measured phase velocity data vs. $\ln(T/T_c)$, normalized at $T_c/2$, for Nb (+), in situ YBCO films on MgO (solid and open circles) and LaAlO_3 (square) and BCS theory (line).

strates show values of n ranging from 1.3 to 3.2 [82,83].

The variations in the measured temperature dependence of $\lambda(T)$ suggest that an extrinsic mechanism is responsible for these observations. Anlage et al. have proposed that grain boundary weak links are responsible for limiting the high frequency shielding currents and changing the temperature dependence of $\lambda(T)$ [82,83]. Figure 25 suggests that the influence of grain boundary weak links on $\lambda(T)$ may be

stronger for films grown on LaAlO_3 than for those grown on MgO.

Although in principle the microstrip resonator technique can be used to measure the absolute magnitude of λ , in practice uncertainties about the dielectric constant of the transmission line prevent one from directly calculating λ [82–84]. We have developed a technique to obtain $\lambda(T)$ over the entire temperature range by fitting the data to a theoretical expression for $\lambda(T)$ and using T_c and $\lambda(0)$ as fitting parameters [82–84]. The values obtained for $\lambda(0)$ depend strongly on the form of the temperature dependence used to fit the raw data. Table V shows the values of $\lambda(0)$ obtained from two different temperature dependences: Gorter–Casimir (two-fluid model) and BCS weak coupling theory as tabulated by Muhlshlegel [85]. The trends seen in the data hold true for penetration depths obtained by either type of analysis.

As with the surface resistance, we wish to relate the penetration depth results with the normal state properties of the films. The normal state transport properties are known to be influenced by the percolating conducting paths created by insulating boundaries or misaligned grains in thin films. This has the effect of increasing the path length and reducing the cross-sectional area for current flow, resulting in an enhancement of the resistivity [86]. At high frequencies, current path lengthening may not be the correct description for enhanced inductance. Instead, RF current may be forced through weak links that DC currents do not probe. These currents produce a contribution to the inductance from the weak link inductance. A measure of this enhanced inductance of a film is given by the inductivity [83,84].

$$\mathcal{L}_{\text{film}}(0) = \mu_0 \lambda^2(0). \quad (9)$$

An ideal YBCO film ($\lambda(0) = 1400 \text{ \AA}$) will have an inductivity of $\mathcal{L}_{\text{film}}^{\text{ideal}}(0) = 2.5 \times 10^{-10} \text{ H\AA}$. Measured values of the inductivity will be enhanced above this ideal value [83], and should increase with the normal state resistivity. To demonstrate this, we plot the inductivity (calculated from $\lambda_{\text{BCSM}}(0)$) versus the normal state DC resistivity at 100 K in fig. 26(a) and (b). Excluding the right-most point, which represents the primarily a -axis normal oriented film, the inductivity is a strong function of the normal state resistivity. It is not surprising that the residual in-

Table V

Results of penetration depth measurements on in situ sputtered YBCO thin films. Penetration depth $\lambda(T)$ was obtained by a Gorter-Casimir (two-fluid) fit (λ_{CG}) and a BCS (Muhlshlegel) fit (λ_{BCSM})

Sample #	Substrate	Texture	T_c (K) ($R=0$)	T_c (K) BCS M fit ($1/\lambda=0$)	ρ_{100} ($\mu\Omega\text{cm}$)	$d\rho/dT$ ($\mu\Omega\text{cm/K}$)	$\rho(0)$ ($\mu\Omega\text{cm}$)
250B5	LaAlO ₃	<i>c</i>	87.5	87.5	150	1.4	10
64B5	MgO	<i>c</i>	80.6	80.3	150	1.1	40
127B5	LaAlO ₃	10% <i>a</i> +90% <i>c</i>	74.0	71.6	175	1.6	15
202B6	LaAlO ₃	70% <i>a</i> +30% <i>c</i>	77	74.8	350	1.5	200
M058C56	MgO	<i>c</i>	84		100	0.8	18
214C34	MgO	<i>c</i>	67	65.1	200	0.8	110
M058C45	MgO	<i>c</i>	80	80.7	120	1.0	20

Thickness (Å)	Substrate temperature (°C)	Critical current (A/cm ²)	R_s at 4.2 K and 10 GHz ($\mu\Omega$)	$\lambda_{CG}(0)$ (Å)	$\lambda_{BCSM}(0)$ (Å)	$\mathcal{L}_{CG}^{\text{film}}(0)$ ($\times 10^{-10}\text{H}\text{\AA}$)	$\mathcal{L}_{BCSM}^{\text{film}}(0)$ ($\times 10^{-10}\text{H}\text{\AA}$)
780	730			3690	2400	17.7	7.5
2400	650	1×10^7		2960	2040	11.4	5.4
2400	660			4570	3010	27.2	11.8
2000	640			6290	3630	51.5	17.2
4010	700	4×10^7	16	2170	1360	6.1	2.4
5440	650	4×10^6	744	6360	4070	52.7	21.6
4340	700	4×10^7	26	1900	1340	4.7	2.33

ductivity scales with the normal state transport properties since these properties, as well as the residual surface resistance, are known to be affected by the presence of grain boundaries. These grain boundaries are expected to add an effective inductance to the film. It should be noted that films with the lowest zero-temperature inductivity also correspond to those with the smallest residual surface resistance at 10 GHz.

4. Conclusion

High quality epitaxial YBCO films can be grown by 90° off-axis single magnetron sputtering technique at intermediate pressures and relatively low substrate temperatures. The best films are comparable to the best single crystals in transport and sharpness of transitions. Optimum values for surface resistance, penetration depth and smoothness are found in samples with T_c 's slightly lower than bulk values and with the *c*-axis lattice parameters slightly longer. It has not yet been determined why T_c is slightly lower and the *c*-axis is slightly expanded but

those properties are not due to oxygen deficiencies at the chain sites. The low temperature growth of thin films introduces fine-scaled disorder. We have investigated the growth kinetics and the various defect structures in the in situ grown films by microstructural studies with TEM and X-ray diffraction. If a significant density of defects affects the oxygen "bridge" sites for example they could account for the increased *c*-axis lattice parameter and act as additional pinning sites without increasing the resistivity appreciably. The large normal state conductivity, high critical current density and constant near-single-crystal value of the *a*-axis lattice parameter support the idea that the CuO₂ planes are left mainly intact. The fact that ultra-thin superconducting films below 20 Å can be grown sets a limit on substrate-film interaction. Superior but far from ideal RF properties suggest relatively clean grain boundaries and a high degree of epitaxy.

Acknowledgements

We gratefully acknowledge the encouragement and

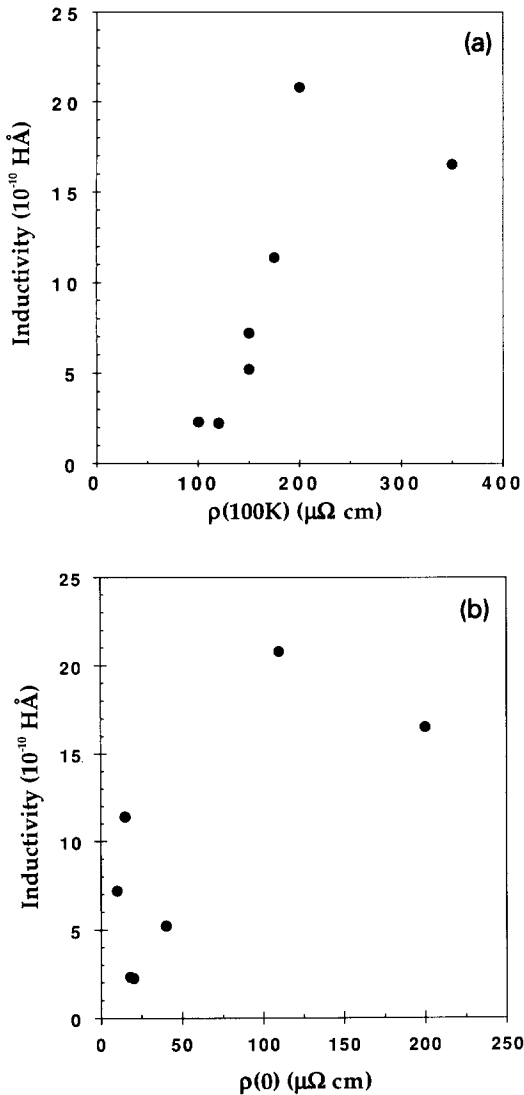


Fig. 26. (a) Thin film inductivity (BCSM) at zero temperature, for YBCO films vs. their normal state resistivity at 100 K, $\rho(100$ K). (b) Thin film inductivity at zero temperature, for YBCO films vs. their normal state resistivity extrapolated to zero temperature, $\rho(0)$.

support of Profs. Beasley and Kapitulnik and the members of the Stanford Department of Applied Physics KGB group. And, we have also profited from interactions with N. Newman, K. Char and J.M. Rowell. The authors would also like to thank D.L. Keith and W. Holmes for their help in developing the sputtering facility and B.W. Langley for analysis

of the penetration depth data. We also thank S. Johnson and coworkers from SRC. Some of the targets used came from material being studied with S. Johnson under support of EPRI and DARPA. The work at Stanford has been supported in part by the Air Force Office for Scientific Research under contract F49620-88-C-004, by the Stanford Center for Materials Research under the NSF-MRL program, and by the Electric Power Research Institute Grant RP8009-11.

Appendix

Applicability of the Bean model for thin films

The Bean model is based upon the assumptions that self-fields can be neglected and that shielding currents flow macroscopically in the sample. These assumptions will be considered in the following discussion. The applicability of eq. (1) for determining $J_c(H)$ is limited to the range of fields where the internal field in the sample is approximately equal to the applied field throughout that volume of the film which contributes substantially to the observed moment. Otherwise corrections to eq. (1) for the self field are required [87]. The anisotropy of the superconducting properties in our oriented films complicates these self-field corrections, since the self-field affects the local direction of the field at the film surface, as well as the field intensity. We have limited this work to cases where self field corrections are unimportant.

The applied field criterion can be approximately expressed as

$$H^* \ll H_a, \quad (10)$$

which is the criterion described in ref. [89]. H^* is a measure of the field due to the circulating shielding currents, defined as

$$H^* \equiv \frac{4\pi J_c(H) \ell}{c}. \quad (11)$$

For the case $J_c = 5 \times 10^7$ A/cm² and the sample thickness $\ell = 3000$ Å, values applicable to the film in fig. 12 in zero applied field, we obtain $H^* = 1800$ G. The validity of eq. (10) as a criterion for the importance of self-field effects, and the use of eq. (1),

with R chosen as the average radius of the sample, can be assessed by considering the endpoint of the magnetization loop, in fig. 12 at $H = 15$ kG. A simple model which assumes an annular region which shields the center of the disk upon reversal of the field scan direction yields

$$M(H) = M_0 \{1 - 2 \exp(-3(H - H_{\max})/H^*)\}, \quad (12)$$

where M_0 is the moment at the point the field scan direction is reversed, and H_{\max} is the field at which the scan direction is reversed. It is seen that H^* is a measure of the field required to reverse the observed moment of the sample. It should be noted that the assumption of the critical state, i.e. currents which are equal to J_c or zero at all points in the sample, is not realized for thin films. Numerical work [88] has shown that the current front, associated with the partial field penetration, is not abrupt in thin films. A consistency check of the Bean formula can be made by comparing H^* obtained from the value of the magnetization in eq. (1), with the value of H^* obtained in eq. (12). Using the magnetization loop shown in fig. 12, we find that H^* as determined at an applied field of 15 kG from eq. (12) is 733 G, while the value determined from eq. (11) is 565 G. This is a reasonable agreement, given the simplicity of the model which leads to eq. (12). The agreement between these two expressions verifies that the shielding currents circulate on a macroscopic length scale characterized by R , the measured sample radius.

The criterion given in eq. (10) is conservative in that the field generated by the sample is less than H^* in most of the sample volume. In numerical simulations [80] the field generated by the sample is greater than H^* only for $r < 0.1R$; this portion of the sample contributes only about 0.1% of the observed moment even though the maximum field generated by a thin circular disk with the above values is about 10 kG near the center [89].

References

- [1] D. Dijkkamp, T. Venkatesan, X.D. Wu, S.A. Shaheen, N. Jisrawi, Y.H. Min-Lee, W.L. McLean and M. Croft, *Appl. Phys. Lett.* 51 (1987) 619.
- [2] S. Witanachchi, H.S. Kwok, X.W. Wang, and D.T. Shaw, *Appl. Phys. Lett.* 53 (1988) 234.
- [3] T. Terashima, K. Iijima, K. Yamamoto, Y. Bando and H. Mazaki, *Jpn. J. App. Phys.* 27 (1988) L91.
- [4] N. Missert, R. Hammond, J.E. Mooij, V. Matijasevic, P. Rosenthal, E. Garwin, T.H. Geballe, A. Kapitulnik, M.R. Beasley, S.S. Laderman, C. Lu and R. Barton, *IEEE Transactions on Magnetics* 25 (1989) 2418.
- [5] H.C. Li, G. Linker, F. Ratzel, R. Smithey, J. Geerk, *Appl. Phys. Lett.* 52 (1988) 1098.
- [6] R.L. Sandstrom, W.J. Gallagher, T.R. Dinger, R.H. Koch, *Appl. Phys. Lett.* 53 (1988) 444.
- [7] C.B. Eom, J.Z. Sun, K. Yamamoto, A.F. Marshall, K.E. Luther, S.S. Laderman and T.H. Geballe, *Appl. Phys. Lett.* 55 (1989) 595.
- [8] J. Kwo, M. Hong, D.J. Trevor, R.M. Fleming, A.E. White, R.C. Farrow, A.R. Kortan and K.T. Short, *Appl. Phys. Lett.* 53 (1988) 234.
- [9] H. Adachi, K. Hirochi, K. Setsune, M. Kitabatake and K. Wasa, *Appl. Phys. Lett.* 51 (1989) 2263.
- [10] M. Kawasaki, S. Nagata, Y. Sato, M. Funabashi, T. Hasegawa, K. Kishio, K. Kitazawa, K. Fueki and H. Koinuma, *Jpn. J. Appl. Phys.* 26 (1987) L736.
- [11] X.X. Xi, J. Geerk, G. Linker, Q. Li and Meyer, 54 (1989) 2367.
- [12] K. Yamamoto, C.B. Eom, T.H. Geballe, presented at Am. Vac. Soc. Meeting (1989).
- [13] The U.S. magnetron gun used was modified by D.L. Keith (Center for Materials Research, Stanford University) to function at high pressures.
- [14] S.M. Johnson, M.I. Gusman, D. Rowcliffe, T.H. Geballe and J.Z. Sun, *Adv. Ceram. Mater.* 2 (1987) 337.
- [15] Superconductive Components Inc.
- [16] Developed by Conductus, Inc. and available from US. Inc.
- [17] G.K. Whener and D. Rosenberg, *J. Appl. Phys.* 31 (1960) 177.
- [18] N. Newman, K. Char, S.M. Garrison, R.W. Barton, R.C. Taber, C.B. Eom, T.H. Geballe and B. Wilkens, *Appl. Phys. Lett.* 57 (1990) 520.
- [19] R. Bormann and J. Nolting, *Appl. Phys. Lett.* 54 (1989) 2150.
- [20] R.H. Hammond and R. Bormann, *Physica C* 162-164 (1989) 703.
- [21] K. Yamamoto, B.M. Lairson, C.B. Eom, J.Z. Sun, R. Hammond, T.H. Geballe, presented at Electric Chemical Society Meeting in Montreal, May, 1990.
- [22] K. Char, M.R. Hahn, T.L. Hilton, M.R. Beasley, T.H. Geballe, A. Kapitulnik, *IEEE Transactions on Magnetics* 25 (1989) 2422.
- [23] K. Char, N. Newman, S.M. Garrison, R.W. Barton, R.C. Taber, S.S. Laderman and R.D. Jacowitz, *Appl. Phys. Lett.* 57 (1990) 409.
- [24] We thank R. Barrett and C. Quate for the Atomic Force Microscope imaging.
- [25] S.J. Hagen, T.W. Jing, Z.Z. Wang, J. Horvath and N.P. Ong, *Phys. Rev.* B37 (1988) 7928.
- [26] K. Char, M. Lee, R.W. Barton, A.F. Marshall, I. Bozovic, R.H. Hammond, M.R. Beasley, T.H. Geballe, A. Kapitulnik and S.S. Laderman, *Phys. Rev.* B38 (1988) 834.

- [27] W.R. McKinnon, M.L. Post, L.S. Selwyn, G. Pleizier, J. M. Tarascon, P. Barboux, L.H. Greene and G.W. Hull, *Phys. Rev. B* 38 (1988) 6543.
- [28] R.J. Cava, B. Batlogg, S.A. Sunshine, T. Siegrist, R.M. Fleming, K. Rabe, L.F. Schneemeyer, D.W. Murphy, R.B. van Dover, P.K. Gallagher, S.H. Glarum, S. Nakahara, R.C. Farrow, J.J. Krajewski, S.M. Zahurak, J.V. Waszczak, J.H. Marsh, L.W. Rupp Jr., W.F. Peck and E.A. Rietman, *Physica C* 153–155 (1988) 560.
- [29] V. Matijesevic, P. Rosenthal, et al., unpublished.
- [30] K. Char A.D. Kent, A. Kapitulnik, M.R. Beasley and T.H. Geballe, *Appl. Phys. Lett.* 51 (1987) 1370.
- [31] J.C. Bravman and R. Sinclair, *J. Elec. Micro. Tech.* 1 (1984) 53.
- [32] S.K. Streiffer, et al., published in *J. Mater. Res.*
- [33] R. Ramesh, D.M. Hwang, T.S. Ravi, A. Inam, J.B. Barner, L. Nazar, C.Y. Chen, B. Dutta and T. Venkatesan, submitted to *Appl. Phys. Lett.*
- [34] S.S. Laderman, unpublished.
- [35] L.A. Tietz, C.B. Carter, D.K. Lathrop, S.E. Russek, R.A. Buhman and J.R. Michael, *J. Mater. Res.* 4 (1989) 1072.
- [36] B.M. Lairson, et al., to be published.
- [37] C. Barry, *J. Electron Microsc. Tech.* 8 (1988) 325.
- [38] D.M. Hwang, T. Venkatesan, C.C. Chang, L. Nazar, X.D. Wu, A. Inam and M.S. Hegde, *Appl. Phys. Lett.* 54 (1989) 1702.
- [39] C.P. Bean, *Phys. Rev. Lett.* 8 (1962) 250.
- [40] Y.B. Kim, C.F. Hempstead and A.R. Strnad, *Phys. Rev.* 129 (1963) 528.
- [41] J. Manhart, P. Chaudhari, D. Dimos, C.C. Tsuei and T.R. McGuire, *Phys. Rev. Lett.* 61 (1988) 2476.
- [42] V.V. Moshchalkov, A.A. Zhukov, D.K. Petrov, V.I. Voronka and V.K. Yanovskii, preprint.
- [43] E.M. Gyorgy, R.B. van Dover, S. Jon, R.C. Sherwood, L.F. Schneemeyer, T.H. Tiefel and J.V. Waszczak, *Appl. Phys. Lett.* 53 (1988) 2223.
- [44] T.L. Hylton and M.R. Beasley, *Phys. Rev. B*, to be published.
- [45] H. Dersch and G. Blatter, *Phys. Rev. B* 38 (1988) 11391.
- [46] A. Inam, X.D. Wu, L. Nazar, M.S. Hegde, C.T. Rogers, T. Venkatesan, R.W. Simon, K. Daly, H. Padamsee, J. Kirchgessner, D. Moffat, D. Rubin, Q.S. Shu, D. Kalokitis, A. Fathy, V. Pendrick, R. Brown, B. Brycki, E. Belohoubek, L. Drabek, G. Gruner, R. Hammand, F. Gamble, B.M. Lairson and J.C. Bravman, *Appl. Phys. Lett.* 56 (1990) 1178.
- [47] R.F. Kwasnick, F.E. Luborsky, E.L. Hall, M.F. Garbauskas, K. Borst and M.J. Curran, *J. Mater. Res.* 4 (1989) 257.
- [48] T.R. Dinger, T.K. Wrotington, W.J. Gallagher and R.L. Sandstrom, *Phys. Rev. Lett.* 58 (1987) 2687.
- [49] J.R. Clem, *Low Temp. Phys.* LT13, 3 (1972) 102.
- [50] For instance, see: *Studies of Critical Currents of Very Thin Multilayered Structures*, EPRI Project 78-22 (1976).
- [51] G. Paterno, C. Alvian, S. Casadio, U. Gambardella and L. Maritato, *Appl. Phys. Lett.* 53 (1988) 609.
- [52] J. Manhart, P. Chaudhari, D. Dimos, C.C. Tsuei and T.R. McGuire, *Phys. Rev. Lett.* 61 (1988) 2467.
- [53] D. Dew-Hughes, *Philos. Mag.* 25 (1974) 293.
- [54] R.T. Kampwirth and K.E. Gray, *IEEE Trans. Magn.* MAG-17 (1981) 565.
- [55] R.T. Kampwirth, D.W. Capone II, K.E. Gray and A. Vicens, *IEEE Trans. Magn.* MAG-21 (1985) 459.
- [56] M. Tinkham and C.J. Lobb, *Solid State Phys.* 42 (1989) 91.
- [57] M. Tinkham, *Introduction to Superconductivity*, McGraw-Hill, New York (1975).
- [58] Y. Yeshurun and A.P. Malozemoff, *Phys. Rev. Lett.* 60 (1988) 2202.
- [59] M.V. Feigel'man, V.B. Geshkenbein, A.I. Larkin and V.M. Vinokur, *Phys. Rev. Lett.* 63 (1989) 2303.
- [60] S. Doniach, Report for the Los Alamos Symposium, December 1989.
- [61] B.M. Lairson, S.K. Streiffer, C.B. Eom and T.H. Geballe, to be published.
- [62] E.J. Kramer, *J. Appl. Phys.* 49 (1978) 742.
- [63] E.H. Brandt, *Phys. Rev. Lett.* 57 (1986) 1347.
- [64] S. Tahara, S.M. Anlage, J. Halbritter, C.B. Eom, D.K. Fork, T.H. Geballe and M.R. Beasley, *Phys. Rev. B* 41 (1990) 11203.
- [65] C.B. Eom et al. *Physica C* 162–164 (1989) 605.
- [66] J.Z. Sun, K. Char, M.R. Hahn, T.H. Geballe and A. Kapitulnik, *Appl. Phys. Lett.* 54 (1989) 663.
- [67] Y. Hidaka, Y. Tajima, A. Katsui, Y. Hidaka, T. Iwata and S. Tsurumi, *Phys. Rev. B* 36 (1987) 7199.
- [68] M. Tachiki and S. Takahashi, *Solid State Commun.* 70 (1989) 291.
- [69] J.Z. Sun, C.B. Eom, B.M. Lairson, J.C. Bravman and T.H. Geballe, to be published.
- [70] D.P. Hampshire and Jones, *Phys. Status Solidi B* 141 (1987) 229.
- [71] W.H. Warnes and D.C. Labalestier, *IEEE Trans. Magn.* MAG-23 (1987) 1183.
- [72] J.R. Fraser, T.R. Finlayson and T.F. Smith, *Physica C* 159 (1989) 70.
- [73] J.Z. Sun and T.H. Geballe, unpublished.
- [74] W. Wkin, *Cryogenics* 27 (1987) 603.
- [75] D.P. Hampshire and H. Jones, *J. Phys. C* 20 (1987) 3533.
- [76] R.C. Taber, *Rev. Sci. Instrum.*, to be published.
- [77] S. Sridhar, D.-H. Wu and W. Kennedy, *Phys. Rev. Lett.* 63 (1989) 1873.
- [78] J.P. Turneaure and I. Weissman, *J. Appl. Phys.* 39 (1968) 4417.
- [79] S.S. Laderman, R.C. Taber, R. Jacowitz, C.B. Eom, T.L. Hylton, A.F. Marshall, M.R. Beasley and T.H. Geballe, *Phys. Rev. B*, to be published.
- [80] S.M. Anlage, H. Sze, H.J. Snortland, S. Tahara, B. Langley, C.B. Eom, M.R. Beasley and R.C. Taber, *Appl. Phys. Lett.* 54 (1989) 2710.
- [81] S.M. Anlage, B. Langley, J. Halbritter, S. Tahara, H. Sze, N. Switz, C.B. Eom, H.J. Snortland, R.C. Taber, T.H. Geballe and M.R. Beasley, *Physica C* 162–164 (1989) 1645.
- [82] S.M. Anlage, B.W. Langley, H.J. Snortland, C.B. Eom, T.H. Geballe and M.R. Beasley, presented at the Symposium on High Temperature Superconductors in High Frequency

- Fields, March, 1990. To be published in the October, 1990 issue of *J. Superconductivity*. 3 (1990) 311.
- [83] S.M. Anlage, B.W. Langley, J. Halbritter, C.B. Eom, N. Switz, T.H. Geballe and M.R. Beasley, presented at the Spring MRS Meeting, Symposium S, San Francisco, April, 1990.
- [84] B.W. Langley, et al., unpublished;
S.M. Anlage, et al., presented at Int. Conf. on Low Temp. Phys. 1990 (Brighton, England).
- [85] B. Muhlshlegel, *Z. Phys.* 155 (1959) 313.
- [86] J. Halbritter, *Int. J. Mod. Phys.* 3 (1989) 719.
- [87] David J. Frankel, *J. Appl. Phys.* 50 (1979) 5402.
- [88] M. Däumling and D.C. Larbalestier, *Phys. Rev. B* 40 (1989) 9350.
- [89] J.Z. Sun, Ph.D. Thesis, Stanford University, (1989).